THE PENNSYLVANIA STATE UNIVERSITY
SCHREYER HONORS COLLEGE

DEPARTMENT OF MECHANICAL AND NUCLEAR ENGINEERING
AND ENGINEERING SCIENCE AND MECHANICS

COMPARATIVE ASSESSMENT OF COLD SPRAY, LASER-ASSISTED COLD SPRAY, AND DIRECT METAL LASER SINTERING OF TI-6AL-4V

MICHAEL J. TROWBRIDGE

SPRING 2017

A thesis
submitted in partial fulfillment
of the requirements
for baccalaureate degrees
in Mechanical Engineering and Engineering Science
with interdisciplinary honors in Mechanical Engineering and Engineering Science

Reviewed and approved* by the following:

Timothy J. Eden
Associate Professor of Engineering Science and Mechanics
Thesis Co-Supervisor

Timothy W. Simpson
Paul Morrow Professor of Engineering Design and Manufacturing
Thesis Co-Supervisor

Sean N. Brennan
Professor of Mechanical and Nuclear Engineering
Honors Advisor

Gary L. Gray
Professor of Engineering Science and Mechanics
Honors Advisor

Judith A. Todd
Department Chair
P. B. Breneman Chair and Professor of Engineering
Science and Mechanics

*Signatures are on file in the Schreyer Honors College and in the Engineering Science and Mechanics office.

ABSTRACT

Ti-6Al-4V is an α-β titanium alloy that continues to be widely used in the aerospace and medical industries due to its corrosion resistance and impressive strength-to-weight ratio. Ti-6Al-4V's high manufacturing time and cost make the alloy an excellent candidate for near-net shape fabrication. However, fabrication processes often introduce thermal effects that transform the microstructure and degrade mechanical properties. Cold spray (CS) avoids such thermal effects by achieving bonding through kinetic energy. However, Ti-6Al-4V's toughness limits particle deformation and leads to deposition porosity. This investigation examines the effects of several parameters on the coating microstructure and porosity, including driving gas selection, hot isostatic pressing, and laser-assisted cold spray (LACS). Furthermore, the porosity and microstructure of the CS and LACS specimens were compared to a Direct Metal Laser Sintering (DMLS) specimen. Ultimately, eight series of specimens were analyzed across a range of fabrication processes, parameters, and post-process conditions. The results provide a better understanding of the microstructure of sprayed and printed Ti-6Al-4V and form a foundation for future mechanical testing of these processes.

KEYWORDS: cold spray, laser-assisted cold spray, direct metal laser sintering, selective metal sintering, titanium, Ti-6Al-4V**,** additive manufacturing, characterization, porosity, microstructure, hardness.

Table of Contents

List of Figures

List of Tables

LIST OF ABBREVIATIONS

AM	Additive Manufacturing
ARL	Applied Research Laboratory
ARL	Army Research Laboratory
AM	Additive Manufacturing
CIMP-3D	Center for Innovative Materials Processing through Direct Digital Deposition
CS	Cold Spray
DMLS	Direct Metal Laser Sintering
EBM	Electron Beam Melting
HIP	Hot Isostatic Press
HVN	Vickers hardness number
LACS	Laser-Assisted Cold Spray
MPG	Main Process Gas
OM	Optical Microscopy
PBF	Powder Bed Fusion
PSU	Pennsylvania State University
SLS	Selective Laser Sintering
Ti-6Al-4V	Titanium - 6 Aluminum - 4 Vanadium
WPI	Worcester Polytechnic Institute

Acknowledgements

This research would not have been possible without the extensive support and professional collaboration that was generously offered to me. First, I would like to thank Dr. Timothy J. Eden of the Applied Research Lab (ARL) and the Engineering Science and Mechanics Department and Dr. Timothy W. Simpson of the Mechanical and Nuclear Engineering Department for serving as my co-supervisors on this research. I would like to thank the Worcester Polytechnic Institute (WPI), MOOG, the Army Research Lab (ARL), and VRC Metal Systems for their support in fabricating the cold spray and laser-assisted cold spray specimens. Likewise, I would like to thank Dr. Ted Reutzel and the Center for Innovative Materials Processing through Direct Digital Deposition (CIMP-3D) for printing the direct metal laser sintering specimen.

I would also like to thank Chris Wertz and Dr. Jeremy Schreiber of ARL for their help with etching and microstructure analysis. I also thank Edward Good of the Materials Research Institute (MRI) for his help in microhardness testing. Finally, I would like to thank Aaron Birt of WPI and Victor Champagne and Dennis Helfritch of the Army Research Lab for their technical advice on cold spray and laser assisted-cold spray.

Chapter 1
Introduction

1.1 Motivation

Titanium and its alloys have established a strong foothold in the medical, marine, and aerospace industries due to their excellent ratio of tensile strength to density and high corrosion and fatigue resistance [1-2]. In particular, α-β titanium alloy Ti-6Al-4V has excellent mechanical properties and is found in many modern rotorcraft and airplane components, including rotors, compressor blades, and nacelles [1]. Although Ti-6Al-4V parts have been traditionally manufactured through subtractive manufacturing, such processes incur high machining costs and discard costly scrap material. This high processing cost makes Ti-6Al-4V a strong candidate for additive manufacturing (AM). A large and diverse family of AM processes have been developed since the 1980s, with each process having a unique set of benefits and drawbacks [3].

One common tradeoff that varies between AM processes is the amount of heat-transfer involved in the process. High temperature technologies, such as powder bed fusion and thermal spray processes, have been able to achieve impressively low porosity but are prone to suffer from thermal effects, such as microstructure phase transformations and residual stress. Alternatively, cold spray (CS) is a solid-state technique that uses kinetic energy rather than thermal energy to achieve deformation and bonding. The resulting advantages include lower residual stress, no phase changes, and lower oxide content in the final deposition [4]. Although CS depositions show reduced thermal effects, the material deposited is prone to moderate to high porosity. In

particular, early efforts of CS with Ti-6Al-4V proved to be challenging due to the alloy's strength, toughness, and low plasticity. As a result, traditional CS produces material with higher porosity than comparable forged and cast parts [4]. This porosity is a key concern for critical components because it can lead to crack propagation and a sharp decrease in the mechanical performance. Fortunately, the CS process can be optimized, and the deposited material heat treated to drastically reduce porosity and improve mechanical properties.

One particularly interesting advancement is the emergence of laser-assisted cold spray (LACS). In LACS, a laser is integrated into the CS system in order to locally heat and soften the depositing powder. By using moderate laser power, LACS may be able to reduce porosity while maintaining relatively low heat input during the process.

Although CS and LACS have been successfully utilized in a wide range of scenarios, additional development is needed before they can be used for widespread applications. However, more traditional print-based AM processes are already being used in industry in fabricating Ti-6Al-4V parts. These powder bed fusion (PBF) processes can take on many names and derivative processes, with one of the most common being Direct Metal Laser Sintering (DMLS) [3]. For this reason, the baseline in this study will be DMLS of Ti-6Al-4V. The results provide a comparison of the characterization of CS and LACS processes to a more widely used AM process.

1.2 Objectives and Impact of Research

The objective in this investigation is to compare and contrast Ti-6Al-4V samples fabricated by CS, LACS, and DMLS. The study will analyze the relationship between process parameters and post-process effects on porosity, microstructure, and hardness. This investigation

focuses primarily on CS and LACS because there is currently a shortage of information on CS and LACS of Ti-6Al-4V in literature, and more research could lead to better realization of the technologies' potentials. Still, the DMLS specimens will provide a critical baseline comparison. No other previous studies have directly compared CS and LACS to DMLS for Ti-6Al-4V. For CS, LACS, and DMLS to continue to grow, researchers must begin to formulate a more holistic approach to characterization of the deposits. This research aims to assist this process. Specifically, the study compares the porosity levels of CS, LACS, and DMLS Ti-6Al-4V under various process parameters and treatments. The investigation also includes a brief analysis of the microstructure and Vickers hardness of the specimens. By doing so, the research provides a foundation for future investigations for tensile testing in order to determine more mechanical properties of CS, LACS, and DMLS fabricated parts with Ti-6Al-4V.

Traditionally, comparative studies require a level of collaboration that is difficult to achieve. However, Penn State's Applied Research Lab and CIMP-3D have partnered to provide an extensive pool of capabilities and expertise, including a half-dozen outside collaborators with state-of-the-art facilities and world-renowned experience in CS, LACS, and DMLS. These contributors include the Worchester Polytechnic Institute (Worcester, MA), VRC Metal Systems (Rapid City, SD), MOOG Inc. (Buffalo, NY), the Army Research Laboratory (Adelphi, MD), the Applied Research Lab (State College, PA), and CIMP-3D (State College, PA). In particular, WPI, VRC, and MOOG assisted with the spraying of the CS and LACS parts, and CIMP-3D printed the DMLS part. The Army Research Lab and the Applied Research Lab provided expertise and technical assistance, and the Applied Research Lab's Metals and Ceramics Department oversaw management of the investigation.

In the next chapter, the processes, parameters, and microstructure of Ti-6Al-4V are discussed. The chapter opens with an overview of the history and microstructure of Ti-6Al-4V. Then, the CS process is introduced, including the primary process parameters, microstructure of CS fabricated Ti-6Al-4V parts, and the development of LACS. Finally, the chapter discusses the DMLS process, including process optimization and microstructure of AM parts with Ti-6Al-4V.

Chapter 2
Ti-6Al-4V: Processes, Parameters, and Microstructure

2.1 Overview of Ti-6Al-4V

2.1.1 History of Titanium and Its Alloys

Titanium (Ti) was first discovered in 1791 by British reverend and mineralogist William Gregor [2]. Titanium only began enjoying significant prominence in 1910, when Mathew Hunter of Rensselaer Polytechnic Institute successfully isolated it from titanium tetrachloride [2]. By 1932, titanium was extracted commercially and, following World War II, titanium alloy parts were being developed for the aerospace and chemical industries. Since then, Ti-6Al-4V and its alloys have found prominence in many other industries, including architecture, chemical processing, medicine, power generation, marine and offshore, sports and leisure, medical implants, and transportation industries [2]. Titanium alloys are used largely due to their excellent strength-to-weight ratio and superb corrosion resistance. With under half the weight of steel and Ni-based superalloys, Ti-6Al-4V has become a crucial material for weight-sensitive vehicles and devices, including aircraft, ships, and medical implants [2].

2.1.2 Microstructure of Ti-6Al-4V

Pure titanium is allotropic and may exist in an α-phase, β-phase, or α/β-phase. In the α-phase, pure titanium has a hexagonal close-packed (hcp) crystal structure, as opposed to the β-phase, which has a body-centered cubic (bbc) crystal structure. At room temperature, titanium exists in the α-phase, but it undergoes an allotropic transformation to the β-phase when heated to approximately 882 °C.

When pure titanium undergoes phase transformation, a fraction of the original phase remains, resulting in the α/β-phase. However, the exact phase composition and the phase transformation temperature can be altered through the addition of alloying elements. Some alloying elements, known as α stabilizers, increase the phase transformation temperature. Alpha stabilizers tend to be transition metals, such as aluminum, or interstitial elements, such as oxygen. Titanium alloys with stabilizers are characterized by high strength, toughness, creep resistance, weldability, and the ability to retain desirable properties at cryogenic temperatures. Conversely, β stabilizers, such as molybdenum and vanadium, lower the transus temperature. β alloys are heat treatable and are generally weldable. However, the bbc crystal structure in β alloys leaves them susceptible to ductile-brittle transformation and offers poor performance under low-temperature conditions. α/β-phase titanium alloys are desirable because they can offer a compromise between the properties found in the α-phase and β-phase.

Ti-6Al-4V is the most commonly used α/β titanium alloy, accounting for more than 50% of global titanium tonnage [1]. In Ti-6Al-4V, the 6% aluminum serves as the α stabilizer, and the 4% vanadium serves as the β stabilizing element. Similar to pure titanium, Ti-6Al-4V exists primarily in the α-phase at room temperature, although pocket concentrations of vanadium may result in a locally stabilized β-phase. The phase transformation temperature of Ti-6Al-4V ranges

from 870 °C to 980 °C, depending on the inclusion of interstitial elements [5]. For example, Figure 1 shows the Titanium-Hydrogen (Ti-H) phase change diagram for pure titanium at a pressure of 1 atm. Note how titanium transforms to the β phase beyond > 300 °C. Also note the change in the β transus temperature, which is the minimum temperature at which a 100-percent β phase can exist. Figure 1 shows how the β transus temperature is dependent upon the inclusion concentration, in this case hydrogen.

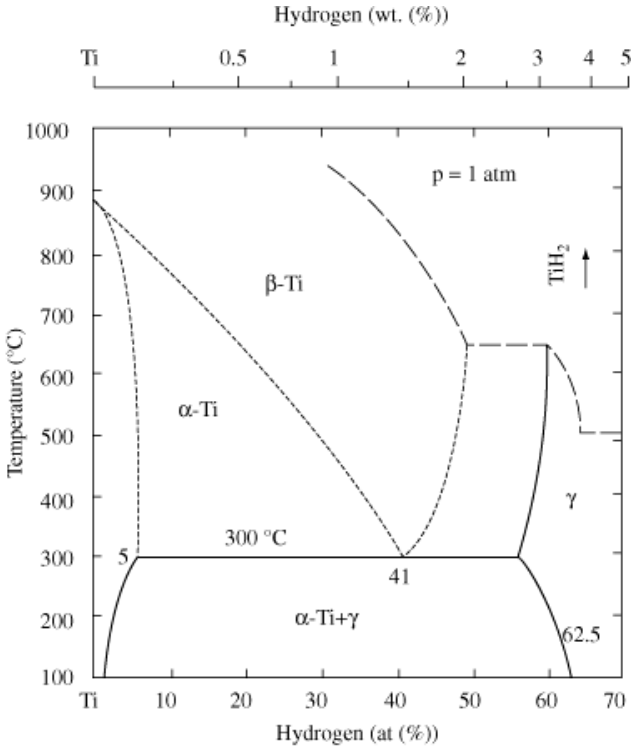

Figure 1. A Ti-H phase change diagram of pure titanium at a pressure of 1 atm [6]

Ti-6Al-4V parts often undergo heat treatment, annealing, hot isostatic pressing (HIPing), or solutionizing and aging treatment. The heat treatment provides stress relieving, annealing improves ductility and machinability, and solution treating and aging improves strength. Additionally, stress relieving and annealing prevent chemical attack [7]. Stress relieving is a

particularly critical process in hot forged, sprayed, and printed titanium parts due to the kinetic and thermal energy involved [5].

2.2 Cold Spray

2.2.1 Basic Principles of Operation

The cold spray process originated during the 1980s at the Theoretical and Applied Mechanics Department of the Russian Academy of Science in Novosibirsk, Russia 87]. While studying supersonic two-phase flow, Papyrin et al. [8] accidentally discovered the potential of solid state deposition of metal powder particles undergoing supersonic velocities. The technology began to gain traction after a U.S. patent was issued in 1994. Soon afterward, a consortium of companies began investigating the technology, including Ford Motor Company, General Motors, General Electric, and Pratt & Whitney [8]. The technology soon gathered a significant research following and continues to grow today.

The basic principles of operation of cold spray are relatively uncomplicated at an introductory level and are demonstrated in Figure 2. A high pressure (up to 4 MPa) inert gas, typically nitrogen (N_2) or helium (He), is directed into two gas streams. One of the gas streams is fed to the feedstock powder feeder, where the feedstock powder particles are entrained into the carrier gas stream. The other stream of main process gas is heated to temperatures between 25 °C to 800 °C. The two streams meet within a delaval converging-diverging nozzle, and the particle-carrier gas stream is accelerated to supersonic velocities. If the velocity meets or exceeds a material-dependent critical velocity, then the powder particles undergo plastic deformation upon

impact with the substrate. The plastic deformation causes mechanical interlocking, and the particles bond in a process similar to cold welding.

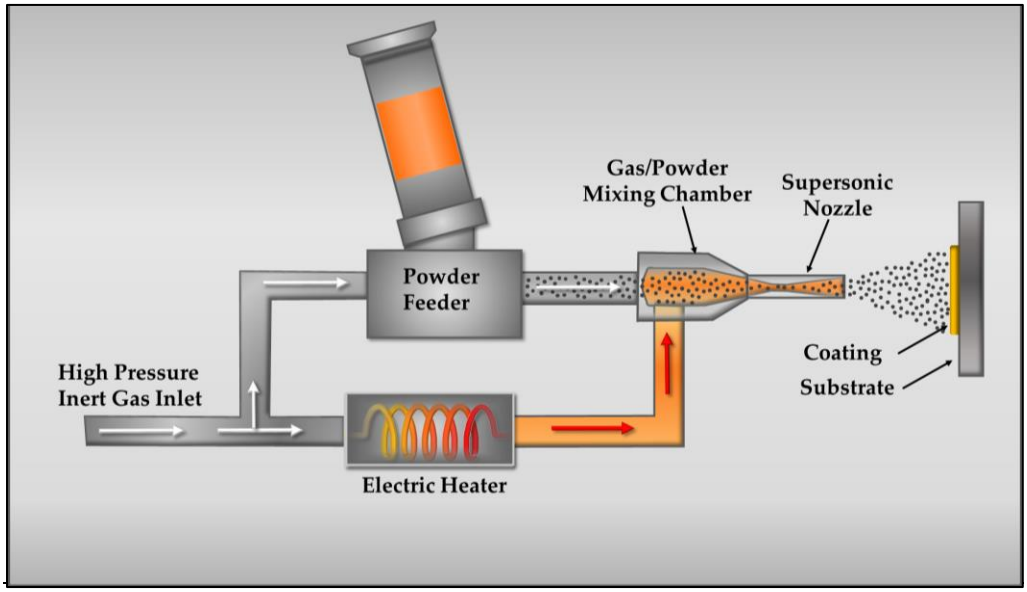

Figure 2. The basic principles of operation of the cold spray process

Although the carrier-gas stream is heated, cold spray is a low heat-exchange process relative to traditional thermal spray technologies, such as plasma arc, wire arc, wire flame, and high velocity oxygen fuel (HVOF). Cold spray's distinctly low process temperature can be clearly seen in Figure 3, which compares the gas temperatures and velocities for various spray processes. Cold spray achieves its low thermal exchange because of its defining characteristic of achieving bonding energy through kinetic energy rather than thermal energy. This serves as cold spray's primary advantage. In thermal spray processes, the depositing particles are melted during deposition and solidify after deposition [1]. This leads to high thermal effects that can cause high residual stresses, porosity, and poor mechanical properties. In contrast, cold spray is a solid-state process in which the material system does not undergo a liquid to solid phase transformation and largely retains its microstructure and mechanical and chemical properties. These benefits make cold spray an attractive option when seeking to avoid thermal effects.

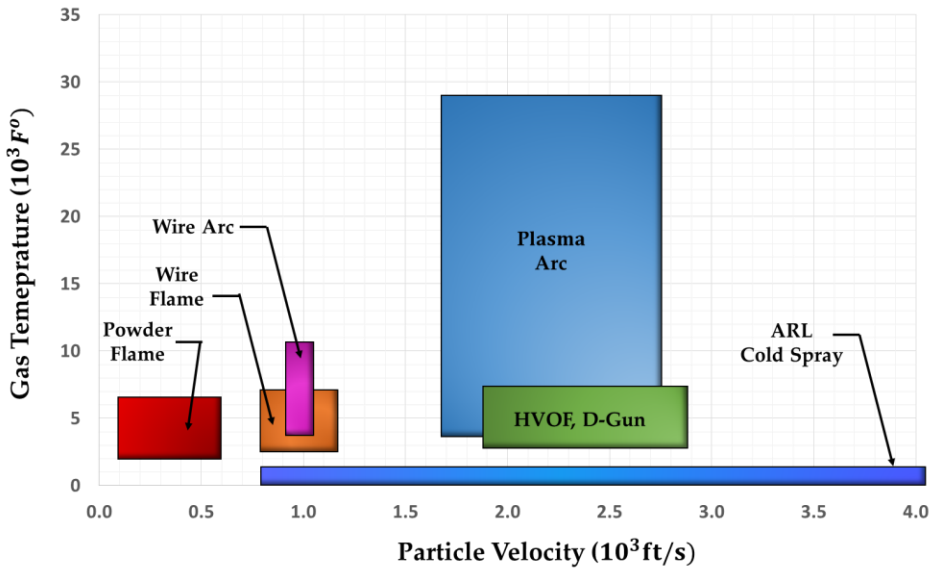

Figure 3. The cold spray process has a significantly lower gas temperatures compared to thermal spray processes

2.2.2 Governing Parameters

Although cold spray's basic principles of operation are easy to grasp, a large number of nuances make CS significantly more complicated in practice. As such, researchers are still working to develop a more encompassing model of the CS bonding mechanics and studying how the deposition is influenced by various process parameters [9-10]. Table 1 summarizes some of the components and parameters investigated in recent optimizing studies on CS depositions. Table 1 is by no means an exhaustive collection of CS parameters, but it provides a simplified overview of some of the components and parameters that must be considered. In particular, this thesis compares specimens produced with different laser powers (for the LACS specimens), exit temperatures and pressures, carrier-gas selection, and heat treatments.

Table 1. An overview of some of the processes and parameters optimized for CS depositions

System Components	Job & Spray Parameters	Preparation & Treatment
Integrated Laser System	Exit Temperature	Substrate Grit Blasting
Delaval Nozzle Geometry	Exit Pressure	Substrate Chemical Cleaning
Helium Recovery System	Type of Process Gas	Stress Relieving
Preheat Chamber	Stand-Off Distance	Hot Isostatic Pressing
	Transverse Nozzle Speed	
	Number of Passes	
	Substrate-Coating Material System	
	Substrate-Coating Material System	
	Particle Size Distribution	

Main Process Gas Selection:

Selection of the main process gas (MPG) is commonly dictated by economic constraints and the critical velocity of the powder particles [2], with nitrogen and helium being the two most common. Nitrogen is the more economical of the two gasses, with the cost of N_2 being more than an order of magnitude lower than helium (He). N_2 produces high quality coatings for many of CS's common material systems. However, the use of N_2 often results in low deposition efficiencies, higher porosity, and lower bond strength compared to He. He's low molecular weight enables the gas stream to achieve a much higher velocity, thus giving the powder more kinetic energy for bonding and deformation. As a result, He depositions often exhibit lower porosity and better mechanical properties. If the CS system supports dual gas streams, then a N_2-He blend may be used to improve performance while reducing the cost of the process gas. Alternatively, a He recovery system can lower operating costs by venting the CS chamber to recycle helium with sufficient purity [12].

Exit Temperature & Pressure:

Two of the most widely examined CS parameters are the gas temperature and pressure. The inlet gas temperature and pressure are easily controllable and, along with the nozzle geometry, directly influence the particle critical velocity and temperature [13]. Temperature is an especially interesting parameter since it must be carefully customized for each material system of powder and substrate. Heating the main process gas achieves much higher velocities than at ambient conditions, but excessive temperatures risk melting the powder and introducing unwanted thermal effects [13-14].

The relationship between the MPG throat velocity (V_T) and temperature (T_t) can be modeled by equation (1), where γ is the ratio of gas specific heats, R is the ideal gas constant, and T_t is the gas temperature at the throat [13].

$$V_T = (\gamma\ R\ T_t)^{0.5} \qquad (1)$$

Harminder, et al. [13] confirmed this velocity-temperature relationship by plotting Equation 1 against experimental data, see Figure 4. Note that the y-axis represents critical velocity (V_{cr}), which is the velocity required for bonding and not simply the velocity achieved in these experiments. A lower V_{cr} indicates a lower velocity is necessary to achieve plastic deformation. Figure 4 shows that a higher particle temperature means less kinetic energy is required and corresponds with a decrease in V_{cr}. The trade-off between V_{cr} and mean particle temperature continues to be investigated and must be determined based on the part or coating material system and intended application [11, 14].

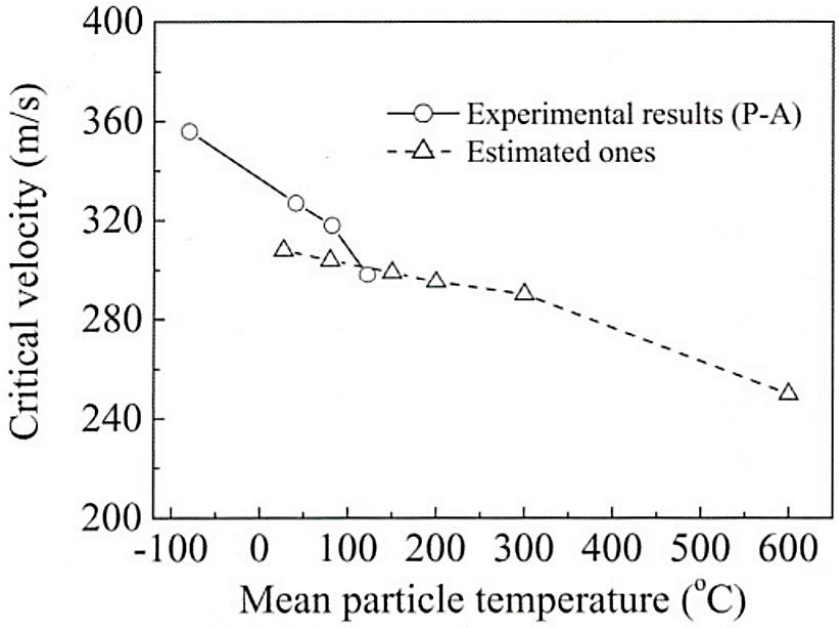

Figure 4. Critical velocity against mean particle temperature [13]

The pressure at the throat shares a similar relationship with gas temperature; higher throat exit pressure results in higher particle velocity. Studies have shown that cold spray has been able to achieve pressures of 10 – 40 bar [4]. Although pressure is often maximized within reason, too high of a pressure may lead to nozzle degradation, particle clogging, and inadequate particle residence time in the nozzle to allow for adequate heating of the particle [4].

Nozzle Design and Stand-Off Distance:

The maximum particle velocity is heavily influenced by even minor changes in the Delaval nozzle design, such as changes in the nozzle's inlet diameter, throat diameter, exit diameter, exit length, and downstream body profile [15-16]. Since many of these dimensions are directly related, it is difficult to analyze one design property in isolation of the other design properties. However, some design parameters can be optimized through experimentation. For example, Ur Rab et al. [17] found that CS sprays using nozzles with exit diameters of 4–10 mm,

throat diameter of 1.5–3 mm, and lengths of 100–200 mm can be used to produce high quality coatings.

Finally, the nozzle standoff distance (distance between the nozzle and the substrate) must be optimized for each material combination. A closer standoff distance allows for a more precise deposition site and decreases particle cooling during travel between the nozzle and the substrate. However, too close of a standoff distance results in excessive heat buildup on the substrate and poor quality deposition [4].

2.2.3 The Laser-Assisted Cold Spray Process

Laser-assisted cold spray (LACS) has been gaining significant attention in recent years as a means to improve the deposition efficiency of the CS process for powders having low ductility [18]. LACS may refer to several laser surface modification methods, including laser surface alloying, laser cladding, laser ablation, and laser heating [18]. For the purposes of this investigation, LACS refers to laser heating, which is the most prominent emerging type of integrated laser system in CS. In LACS, a laser follows the nozzle's spray path. The laser softens the substrate and depositing powder, which increases adiabatic shear stress bonding and mechanical interlocking in the material system. A representation of the LACS process is presented in Figure 5.

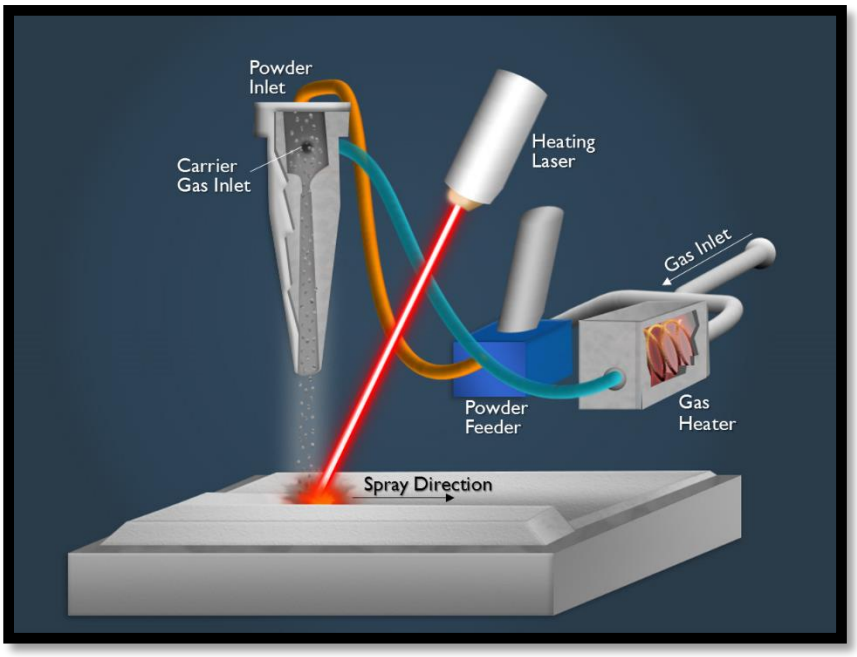

Figure 5. Laser-Assisted Cold Spray combines the benefits of cold spray with laser heating. The heating laser follows the spray path and softens the depositing powder.

The earliest theories on integrating laser into CS were developed by Dykhuizen and Neiser [18] and Sakaki and Shimizu [18]. In particular, Sakaki and Shimizu theorized that deposition efficiency and critical velocity could be improved through moderate laser heating of the impinging particles [18, 19]. Bray et al. [20] demonstrated the technology and went on to create the first fully integrated LACS system, which utilized a diode laser to deposit oxide-free titanium coatings [20]. A brief summary of the LACS process parameters can be found in Table 2.

Table 2. LACS materials and sprayed parameters of Bray et al. [19].

Sprayed material	Ti
Gas	Nitrogen
Gas pressure (MPa)	3.0
Gas temperature (°C)	Unheated (ambient temperature)
Standoff distance (mm)	50
Traverse speed of the gun (mm/s)	500
Passes	1
Laser type	Diode laser (wavelength 890 nm)
Laser power (kW)	< 1

At first, the inclusion of laser heating may seem contradictory to the underlying principle and advantages of CS. However, the laser power in LACS is low enough that the depositing powder does not undergo phase transformations and largely retains its original microstructure, just as it does in CS. Still, the heating and softening is significant enough to improve deposition efficiency, reduce porosity, and improve mechanical properties compared to CS. For example, Lupoi et al. deposited a 4mm titanium coating on carbon steel tubes. A pull-off test recorded an adhesion strength of approximately 77 MPa for the LACS coatings, nearly four times the adhesion strength of CS under comparable process parameters [19].

Although LACS can use carbon dioxide lasers, it more often uses solid state lasers, especially Nd:YAG. The influence of the laser is determined by the laser wavelength, pulse length, beam power, and pulse frequency. The laser system parameters are often customized to be compatible with the depositing material's diffusivity, optical reflectivity, and melting point [18].

2.2.4 Microstructure of Ti-6Al-4V Fabricated with CS and LACS

The basic microstructure of Ti-6Al-4V was introduced in Section 2.1.2 and provides a framework for understanding the microstructure of Ti-6Al-4V fabricated under various deposition processes. The general microstructure effects from CS and LACS are similar and are examined in tandem.

Perhaps the most important attribute of CS and LACS Ti-6Al-4V is that the final deposition largely retains the feedstock powder's original microstructure because the process temperature never exceeds Ti-6Al-4V's transus temperature. Thus, the atomization process and resulting microstructure of the feedstock powder is of great interest for CS and LACS characterization. Aaron Birt of WPI has assisted in this research, having recently published an investigation into the microstructure of feedstock powder used in SC and LACS [21]. The publication included a calculated continuous cooling transformation (CCT) curve shown in Figure 6.

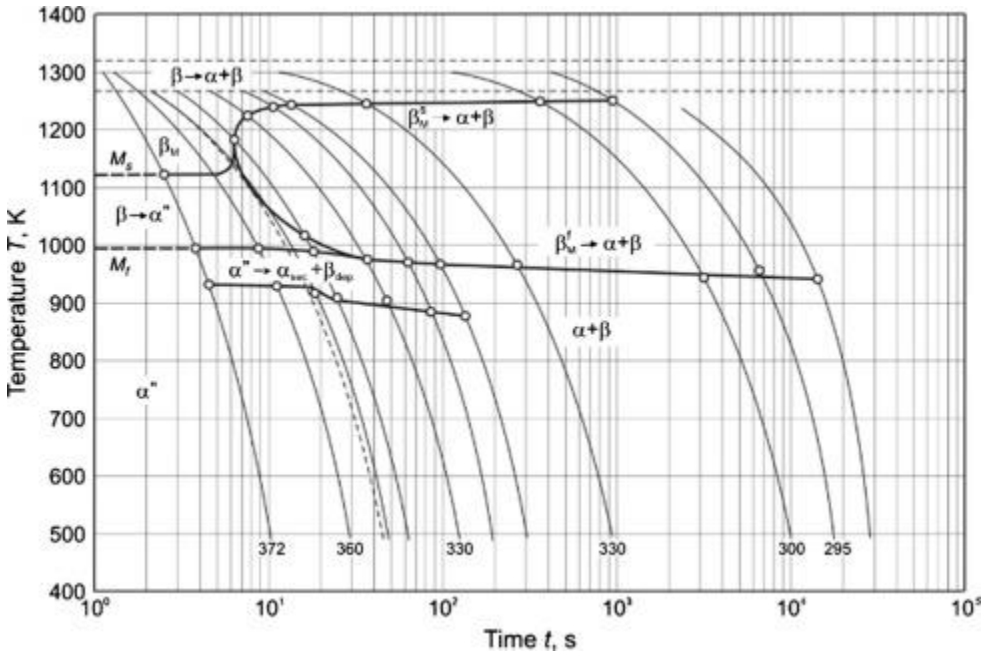

Figure 6. CCT of Ti-6Al-4V [21]

Given the CCT, it is expected that the powder microstructure would be largely dominated by Hexagonal Close Packed (HCP) lathe-like martensitic α' within a matrix of equiaxed α and β phases. The smaller particles cool fast enough that the α' phase does not grow enough to form its characteristic lathe-shape and does not have any organized orientation. These small particles are characterized by a large number of speckled nucleation sites within an α + β phase. The smaller particles appear to have a very fine to structure-less microstructure. However, larger particles cool at a slower rate and may form α' within local sections in the particle. If given enough heat and cooling time, these particles may form an isolated basket-weave martensitic structure. An example of such a particle is shown in Figure 7.

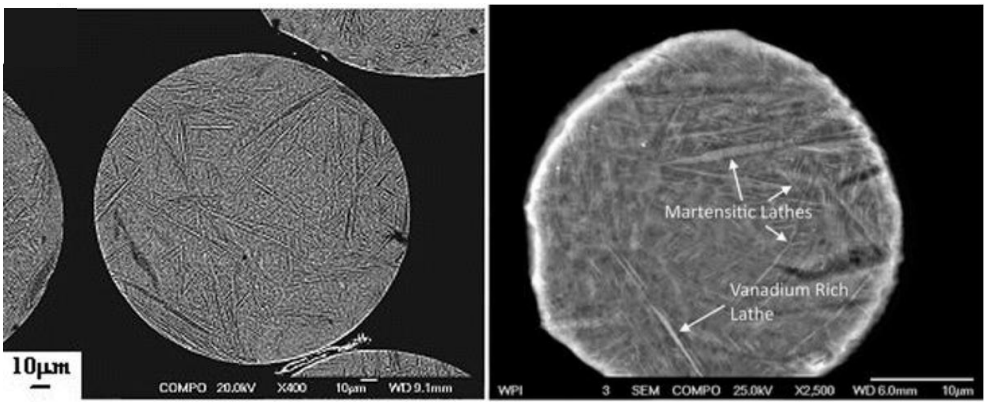

Figure 7. Microstructure of feedstock powder of Ti-6Al-4V [22-23]

Finally, it should be noted that hot isostatic pressing (HIPping) drastically changes the coating microstructure. Zhang et al. [22] found that, depending upon the holding temperate and duration, the martensitic microstructure becomes much more dominant. Micrographs from the study can be found in Figure 7, which shows a clear martensitic α' within an α+ β matrix [22] .

Given the large number of process parameters involved in CS and LACS, the porosity levels can vary widely in Ti-6Al-4V depositions. For example, Moy et al. [24] recorded porosity readings of 12.1%, 9.8%, and 8.9% for cold sprayed Ti-6Al-4V driven by nitrogen. Other studies have shown similar results, with an average area percent porosity of approximately 10% [25]. However, these values have only been achieved through intense optimization efforts. For example, a study by Li et al. [26] was only able to achieve an area percent porosity of 22.3%. In their discussion, Li and his colleagues remark that another study by Blose et al. [26] was able to achieve a lower porosity of 18% by using helium as the MPG instead of nitrogen. In all of these studies, the porosity within the coating depositions varied between ± 5% to nearly ± 10%.

2.3 Direct Metal Laser Sintering

2.3.1 Basic Principles of Operation

Direct Metal Laser Sintering is a derivative technology from stereolithography, the first 3D-printed process. Stereolithography was introduced in the early 1980s by Charles Hull when he used localized heating of thermoplastics to melt concurrent layers of the plastic into desired shapes [27]. Hull immediately recognized the potential of his discovery and formed 3D Systems, which is still an industry leader in additive manufacturing and is credited for establishing the .stl file type [27].

In the early 1990s, the German-based company EOS (Munich, Germany) recognized the emerging market for rapid prototyping. EOS developed their own process and system for selective laser sintering, which they named Direct Metal Laser Sintering (DMLS). DMLS continues to be a frontrunner for commercial selective laser sintering (SLS) and remains closely affiliated with EOS GmbH. [27].

The distinction between DMLS and other powder bed fusion additive manufacturing technologies has been muddied by corporate legality stressing a separation of very similar processes. From a top-level perspective, DMLS is simply a subset technology of Powder Bed Fusion Additive Manufacturing (PBF AM). PBF AM refers to additive manufacturing processes where a laser or electron beam selectively melts and fuses metal powder particles together [28]. After the laser completes the path on the current layer, powder is fed from a hopper and a roller or blade spreads a new layer of powder. The process then repeats, with each consecutive layer forming the neighboring part cross-section. An example system is shown in Figure 8.

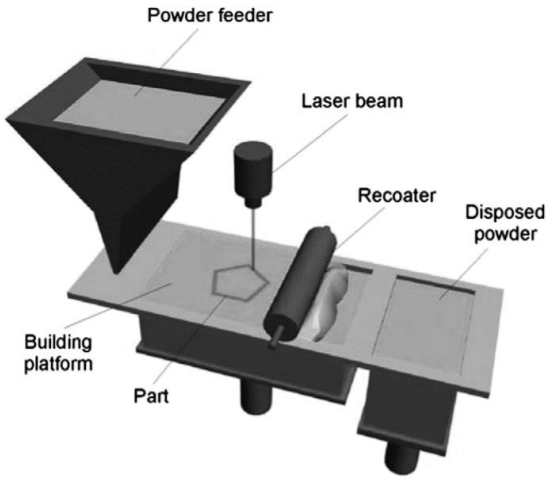

Figure 8. A typical example of a PBF AM system. The laser beam follows the part pattern on the build platform and a recoater disposes the remaining powder [28].

If an electron beam is used, then the process is aptly named Electron Beam Melting (EBM). Developed in 1997 by the Swedish company Arcam AB, EBM has a lower melt scan rate and a different coupling between the beam energy and powder bed compared to laser PBF AM processes [29]. Additionally, EBM parts must be printed under vacuum and may have inferior resolution compared to laser PBF parts [29].

If a laser is used, then the AM technology is known as laser PBF. While EBM is the only commercial electron beam PBF AM process, laser PBF encompasses many trade names, including Selective Laser Melting (SLM), Direct Metal Laser Sintering (DMLS), Laser Cusing, and Selective Laser Sintering (SLS). A level of fluidity exists among these terms, with the most defining distinction oftentimes being the company or patents associated with the process name. Still, differences do exist. While DMLS refers almost exclusively to metal alloys, SLS applies to a broader range of materials, including plastics, glass, and ceramics [29].

2.3.2 Microstructure of DMLS of Ti-6Al-4V

DMLS has garnered significant attention as an AM process for Ti-6Al-4V parts, making it a valuable baseline comparison for CS and LACS. Although DMLS of Ti-6Al-4V is already being implemented commercially, the relationship between processing parameters, microstructure, and mechanical properties continues to be investigated [28]. In particular, many publications focus on the microstructure and porosity of Ti-6Al-4V, as well as how to optimize the DMLS process for the alloy.

One challenge to developing a holistic understanding of DMLS Ti-6Al-4V has been the alloy's non-homogeneity resulting from the microstructure's interdependence on line-wise and layer-wise building strategy. During deposition, the laser heats the target powder to a temperature above the transient temperature, causing the powder to undergo a transformation from the α phase to the β phase. The heat dissipates through the previous layers, accelerating the growth of the grains along the build direction. After the laser leaves the site, the β phase cools and forms α' martensitic grains. Thus, the planes parallel to the build direction show elongated β grains with acicular α' martensitic grains. This delamination can subsequently cause horizontally

orientated pores within the build. A study performed by Tuck et al. [30] investigated this phenomenon in DMLS of Ti-6Al-4V and concluded that the α' martensitic grains may cause delamination between the β grains of neighboring layers.

2.3.4 Optimization of DMLS of Ti-6Al-4V

Because this study includes only one DMLS specimen, the optimization process and parameters of DMLS are not heavily discussed. Still, it is important to understand the key parameters that have been investigated. Studied parameters include the laser angle of incidence, scanning speed, hatch spacing, layer thickness, and laser selection, power, and spot size. A study by Khaing et al. [31] has investigated several of these parameters. For example, a minimum angle of incidence must be found for a successful DMLS deposition. Mechanical properties are also dependent upon hatch distance and scan speed. For DMLS of Ti-6Al-4V, a hatch distance (distance between neighboring print lines) of 0.05 mm to 0.1 mm and a printer head scan speed of 50 mm/s and 100 mm/s produced final percent porosity ranging from 7.3% to 2.5% [31]. The optimal porosity was achieved at a hatch distance of 0.05 mm and a scan speed of 50 mm/s, and the part exhibited a Vickers hardness number (HVN) of 515 [31].

2.4 Summary of Ti-6Al-4V Parts Fabricated With CS, LACS, and DMLS

Previous studies have already proven that Ti-6Al-4V parts can be successfully fabricated through CS, LACS, and DMLS processes. CS is typically better suited for coatings of low to moderate thickness depositions. CS fabricated parts are not subjected to large thermal effects. Consequently, the microstructure and mechanical and chemical properties of the feedstock powder are largely retained in the final deposition. Previous investigations have sought to optimize CS fabrication of Ti-6Al-4V by examining the influence of the MPG, exit temperature and pressure, nozzle design, and stand-off distance. Also, laser heating has recently been investigated as a means of improving the deposition efficiency and decreasing porosity compared to traditional CS fabricated Ti-6Al-4V parts.

DMLS is one of many PBF AM processes. Like other PBF AM processes, DMLS is capable of producing small to large Ti-6Al-4V parts with complex geometries. DMLS parts are prone to non-homogenous microstructure and mechanical properties due to vertical heat dissipation through the previously deposited layers. This phenomenon results in a microstructure dominated by α' martensitic lathe-shaped grains.

Chapter 3

Experimental Procedure and Methodology

3.1 Fabrication of Specimens

A total of six parts were sprayed with CS or LACS using a test matrix developed to compare process type, laser power, heat treatment, and driving gas. Additionally, one part was printed with DMLS. Each part was sectioned to obtain at least two characterization specimens. A minimum of two specimens per part was required in order to examine the porosity and microstructure in both the parallel and perpendicular directions to the spray or print direction. The convention used here is “top” to describe specimens with a polishing plane perpendicular to the spray or build direction and “side” to describe specimens with a polishing plane parallel to the spray or build direction. A summary of the specimens used in each series is shown in Table 3.

Table 3. Summary of Specimen Series

	Operator / Supplier	Process	Laser Power	Post Process Treatment	Driving Gas
Series 1	WPI	CS	0W	None	N_2
Series 2	WPI	LACS	100W	None	N_2
Series 3	WPI	LACS	200W	None	N_2
Series 4	VRC	CS	0W	None	He
Series 5	MOOG	CS	0W	HIP	N_2 (60%) + He (40%)
Series 6	MOOG	CS	0W	HIP	N_2
Series 7	CIMP-3D	DMLS	N/A	Stress Relief	N/A

The majority of the specimens were fabricated using CS (Series 1, 4-6) and LACS (Series 2-3). DMLS served as a baseline comparison and accounted for the final set of specimens (Series 7). Series 1-3 were selected to provide the most direct comparison between CS and LACS, with the primary difference between each specimen set being the heating laser's power; specimens had respective laser powers of 0W (CS), 100W, and 200W. The CS and LACS comparison specimens (Series 1-3) were sprayed at the Worcester Polytechnic Institute (WPI) using a KINETIKS 4000 Cold Gas Spray System (Cold Gas Technologies, Ampfing, Germany). The powder was sprayed on Ti-6Al-4V substrates to study the effects of homogenous substrate-particle pairing on deposition efficiency. Substrates were prepared through grit blasting and surface cleaning using ethanol and acetone. All CS and LACS comparison specimens were sprayed using pure nitrogen as the MPG. The gas temperature at the gun was 750 °C for the entire series of depositions, and an extended preheat chamber was set to 450 °C to ensure that the powder particles reached the set gas temperature before the nozzle exit. The set gas temperature was set high enough to soften the particles, yet low enough to largely avoid thermal effects. An

exit pressure of 30 bar maximized particle velocity while ensuring a reasonable particle flow, and a powder feed wheel rotation of 240 RPM governed the particle flow rate.

A nozzle-substrate standoff distance of 1 inch was selected. Additionally, a raster speed of 200 mm/s and a raster step size of 0.5 mm were selected to ensure that the deposition site experienced adequate laser exposure time without introducing unnecessary localized heating. For the LACS as-sprayed specimens, specimens were deposited using laser powers of 100W and 200W. The powder flow rate (PFR) was decreased from a feeder head rotary speed of 3 rpm for the CS specimens to 1.5 rpm for the LACS specimens to allow the powder adequate exposure to the heating laser. The CS and LACS specimens were sprayed using powder feedstock obtained from Advanced Powders and Coatings Inc. (AP&C) in Boisbriand, Canada. The powder was plasma atomized and contained a particle size distribution certified as 15-45 µm (See Figure 9). The feedstock powder size distribution was certified by AP&C in compliance with ASTM B822-10, with a D10, D50, and D90 of 18.0 µm, 31.6 µm, and 43.5 µm, respectively.

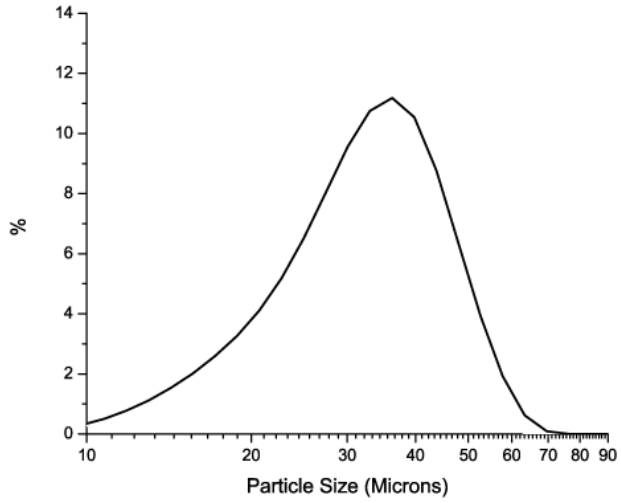

Figure 9. A particle size distribution of the plasma atomized feedstock powder [32]

A helium main process gas (MPG) CS specimen (Series 4) was sprayed to compare the influence of the driving gas on the coating deposition. The He-driven CS specimen shared

similar parameters to those used in the LACS comparison specimens, although minor optimization was done to account for the helium MPG gas. Series 4 was not sprayed at WPI due to equipment complications and a high demand for WPI's KINETIKS 4000 system. Instead, Series 4 was sprayed at VRC systems using their state-of-the-art helium recovery system.

The DMLS specimen (Series 7) was printed at Penn State's CIMP-3D using an EOSINT M 280 DMLS system (EOS, Germany). The laser system used was a YLR-400-SM-EOS with an N_2 Generator and ThermoFlex 2500 chiller. Argon was used as a shielding gas and Ti 0006 was used as the substrate material. Completed parts were removed from the build plate through wire EDM provided by Acura-Cut (Pleasant Gap, PA). Unlike the CS and LACS parts, the DMLS parts were subjected to stress relief in Argon at 650 °C for 3 hours by Solar Atmospheres (Hermitage, PA).

An additional set of CS specimens were subjected to hot isostatic pressing (HIPping) after deposition (Series 5-6). These HIPped specimens were included to better understand the influence of the HIP process and enrich the comparison between CS and DMLS. That is, the stress relief of the DMLS specimen decreases residual stress and eliminate porosity, but complicates the cogency of a direct comparison to as-sprayed CS and LACS. Alternatively, the HIPped specimens allowed for a more holistic comparison to both as-sprayed and application-ready CS.

The HIPped CS specimens were sprayed by MOOG Inc. (East Aurora, NY). MOOG was selected to spray the second series of specimens due to scheduling and maintenance constraints on the CGT-4000 system at WPI. The majority of the system and process parameters remained the same as the as-sprayed specimens. However, Al 6061 substrates were used for the HIPped specimens to provide for better machinability and lower processing costs. Two HIPped

specimens were sprayed – one with a pure nitrogen driving gas and the other with a 60% nitrogen 40% helium driving gas mixture. The HIPping process itself was done at Penn State ARL. A summary of the HIPping conditions can be seen in Figure 10. Specimens were held at 925 °C and 15 ksi for four hours.

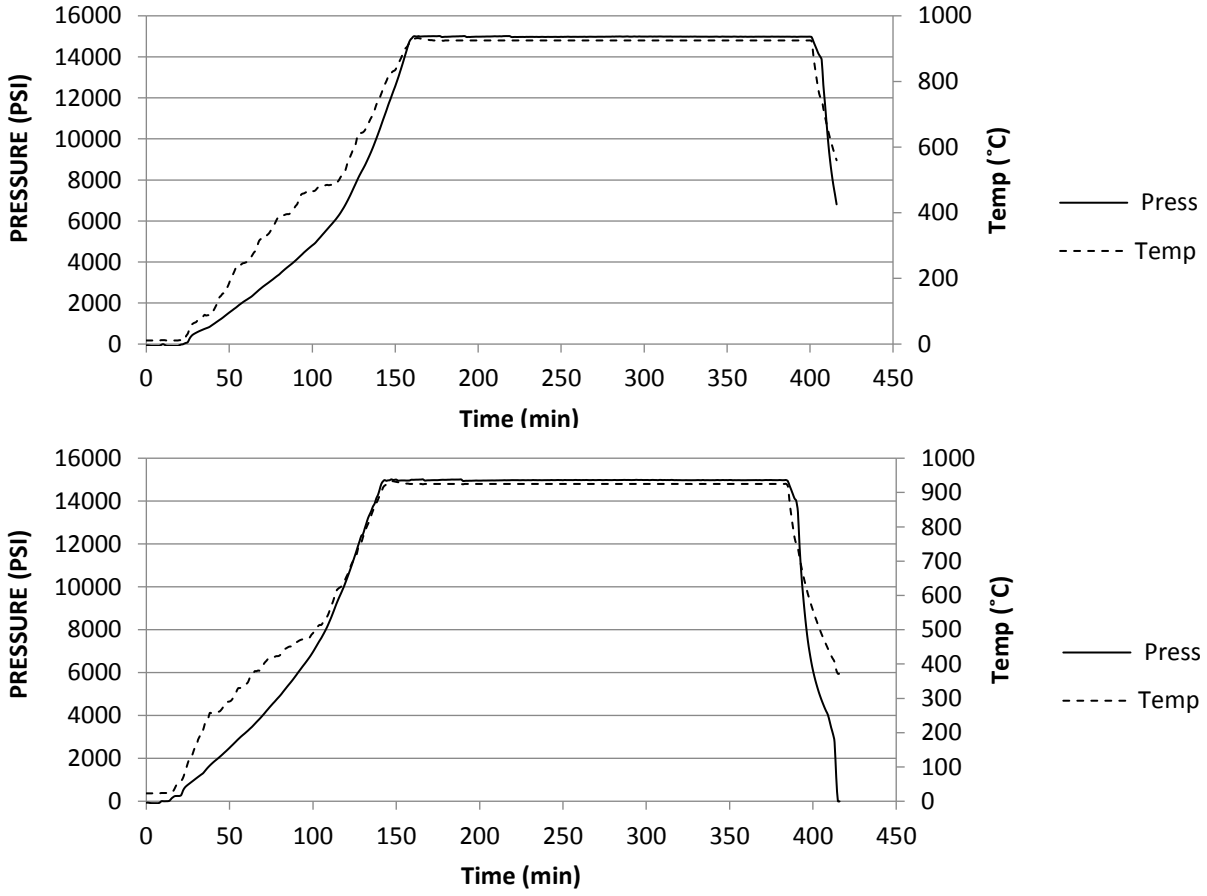

Figure 10. Hot Isostatic Pressing for N_2 (top) and N_2+He-driven (bottom) CS specimens

3.2 Characterization Methodology

After all specimens were sprayed or printed, they were shipped to Penn State ARL for sectioning, mounting, and characterization. Sectioning was accomplished on an ISOMET 1000

Precision Cutter [33-34] using a 5 in diameter and 20 HC wafering blade. A load of 200 lb. was applied under a rotational speed of 650 RPM. The blade had constant cooling from deionized water, and the cutting plane was minimized. Specimens were mounted in MetLab clear casting epoxy using 15 parts (by volume) resin by 2 parts (by volume) hardener. The resin-hardener mixture was subjected to vacuum impregnation using a Struers CitoVac vacuum impregnation unit under 2000 psi for 25 minutes. Afterwards, the mounted specimens were allowed to set for at least 12 hours.

All specimens were polished using a LECO automated polisher system. A four-step polishing recipe was developed based on similar recipes published by Struers and previous investigators [33-34]. First, specimens were flattened on 280 and 320 grit paper with DI water rinsing until plane. Specimens then underwent polishing cycles with a 9µm diamond suspension and a 3µm diamond suspension. The head and disk rotated complementary to each other at 80 rpm and 120 rpm, respectively. For all steps, a head force of 20 lbf was used. Near-polished specimens underwent a final mechanical chemical polishing step using colloidal silica suspension for two to three minutes.

Porosity and microstructure were analyzed using a Nikon Epiphot 200 inverted metallographic microscope. Optical micrographs were captured with a Nikon DS-Fi1 camera head, and image analysis was conducted using NIS Elements (Version 4.51) imaging software. Porosity was recorded through the NIS Element's built-in toolset, which reports an object count using an intensity profile and user-defined threshold. Porosity was estimated from a series of three 100x micrographs. To generate an image of porosity over a larger continuous area, NIS Element's built-in stitching toolset was used to capture the stitched micrograph.

Etching was performed using Kroll's reagent, the most common reagent to use for α-β alloys. Kroll's reagent is comprised of 100 ml deionized H_2O, 3 ml hydrofluoric acid, and 6 ml nitric acid. Specimens were submerged in the reagent for a total of 60 seconds and were examined under an optical microscope in intervals of 10 seconds to check for over-etching.

Microhardness testing was performed using Vickers hardness (HVN) in accordance to ASTM E384-16. The machine model was a V100-C1 (Leco, Japan) with a load of 300 kg and an indentation time of 5 seconds. HVN was averaged from twenty indentation sites randomly dispersed across the entirety of the specimen's polished surface. Additionally, the standard error of the mean was recorded and reported. Test sites maintained a target separation of 1 mm and a minimum separation of at least three times the width of the previous indentation. Test sites were selected to avoid any minor scratches and major pores, although some test sites closely neighbored small pores in the specimens with significant porosity. The results from the characterization and testing are discussed in the next chapter.

Chapter 4

Results and Discussion

In this chapter, the results of the porosity analysis, microstructure characterization, and microhardness testing are presented and discussed. For each topic, both the horizontal and the lateral polishing faces are considered, and the orientation sensitivity is discussed. A collection of comparisons analyze the influence of laser heating, MPG selection, and HIPping on the CS fabricated parts with Ti-6Al-4V. Comparisons are also made to the baseline DMLS fabricated specimen.

4.1 Porosity

Porosity was analyzed for each of the process and parameter conditions in both the horizontal and vertical planes. The results are summarized in Table 4 and discussed in detail following the table. Table 4 provides the average (AVG), standard error of the mean (SEM), and standard deviation (SD) of the porosity measurements.

Table 4. Summary of Area Percent Porosity Analysis (%)

	CS, N2	LACS (100W)	LACS (200W)	HIPped CS, N2	HIPped CS, N2 + He	CS, He	DMLS
	Series 1	Series 2	Series 3	Series 5	Series 6	Series 4	Series 7
	Horizontal Plane (Longitudinal)						
AVG	9.49	9.05	9.20	3.54	0.27	0.07	0.06
SEM	0.61	0.64	0.54	0.27	0.03	0.02	0.01
SD	1.93	2.02	1.72	0.84	0.10	0.05	0.04
	Vertical Plane (Longitudinal)						
AVG	9.62	9.32	9.16	1.59	0.25	0.03	0.01
SEM	0.35	1.09	0.85	0.49	0.14	0.01	0.01
SD	1.12	3.45	2.69	1.55	0.45	0.02	0.03

The results of Table 4 are partially visualized in Figure 11. First, a comparison is made among the N_2-driven CS and LACS specimens. The horizontal plane of the CS Ti-6Al-4V specimen exhibited an 9.49 area percent porosity (See Figure 12). This reading is consistent with the results from previous studies [24-26, 35]. The horizontal plane of the LACS Ti-6Al-4V specimens showed area percent porosities of 9.05% for the 100W and 9.20% for the 200W (See Figure 13). To check the statistical significance of the porosity improvement, a t-test was performed. The LACS specimens showed a t-score of 1.7925 and a two-tailed p-value of 0.0899. By convention, a p-value of 0.05 is indicative of statistical significance, so the improvement in porosity is close to but not quite statistically significant. LACS is still a young technology that has not been thoroughly optimized; so, it is reasonable to expect porosity improvement through future laser optimization efforts. Also note that this study used a relatively conservative laser power of 100W and 200W in order to investigate the onset of thermal effects on the microstructure. If a higher laser power is used, then the LACS process may have a greater porosity reduction over CS.

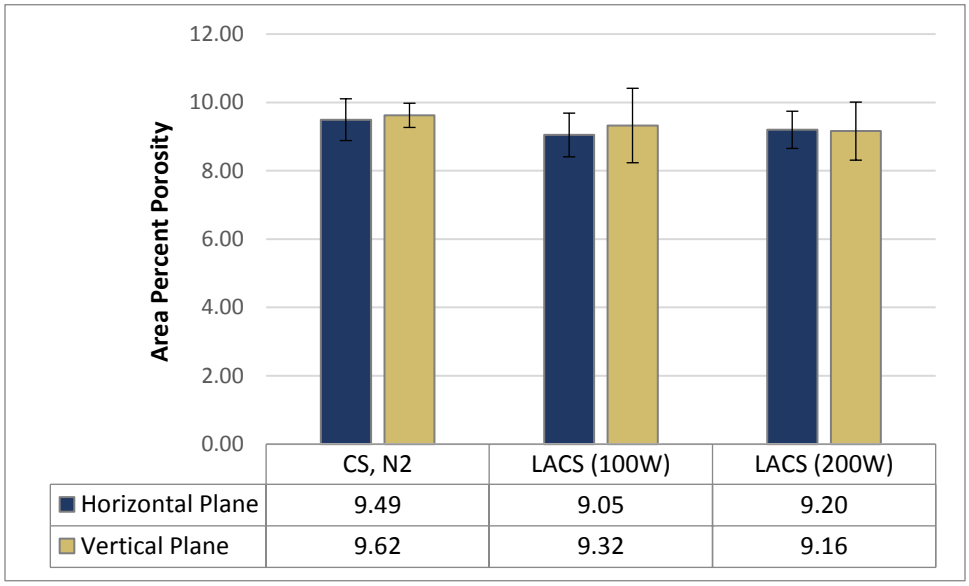

Figure 11. Porosity comparison between CS, LACS (100W) and LACS (200W). The error bars represent the SEM calculated across ten micrographs for each specimen.

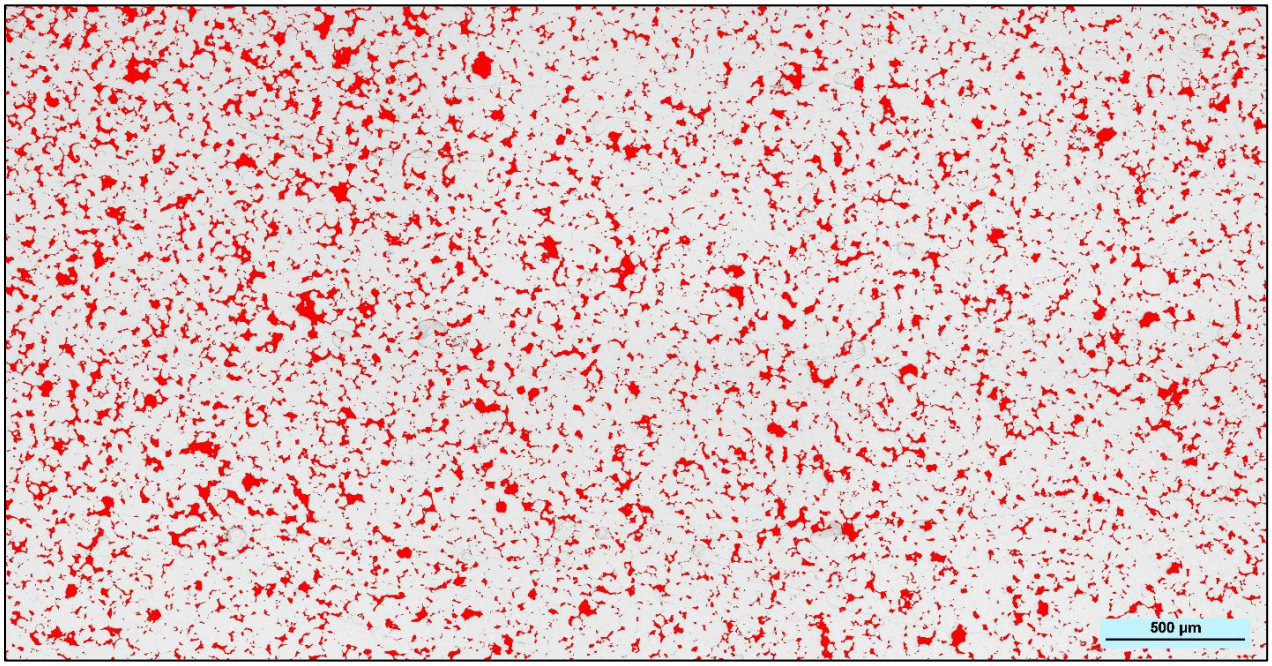

Figure 12. A micrograph of CS Ti-6Al-4V. The specimen was sectioned perpendicular to the spray direction, and the red marks indicate where porosity readings were detected.

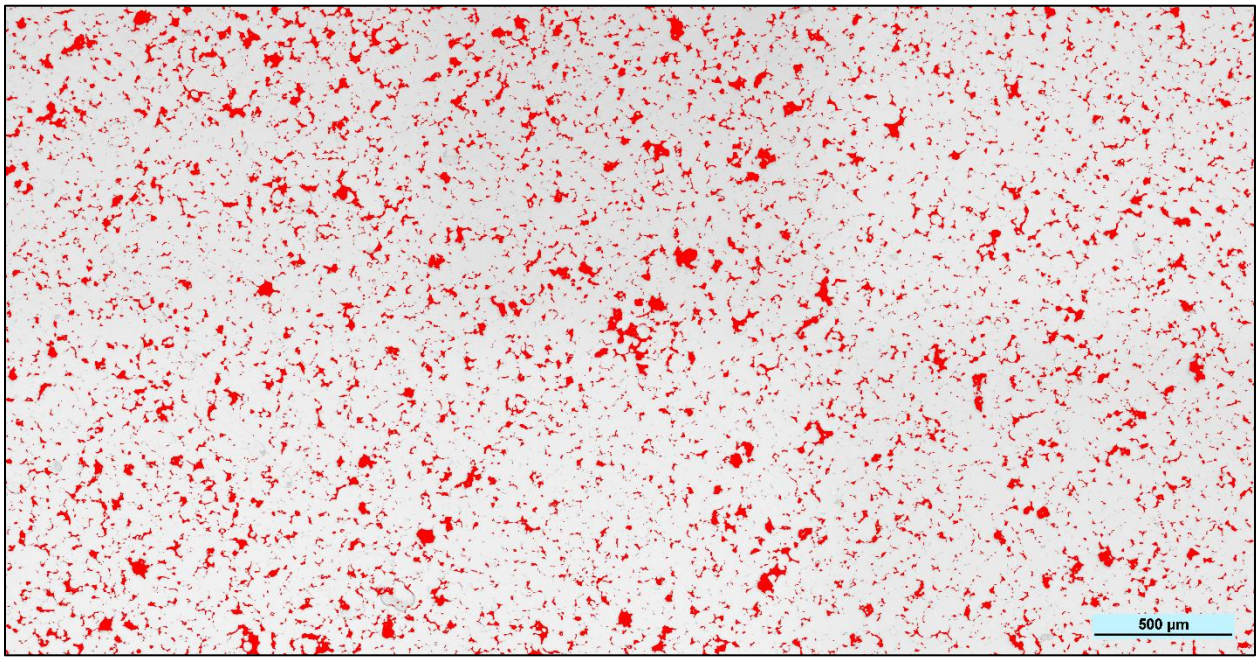

Figure 13. A micrograph of LACS Ti-6Al-4V. The specimen was sectioned perpendicular to the spray direction and porosity readings were burned onto of the micrograph.

Figure 14 shows a summary comparison of the porosity directionality for the N_2-driven CS (See Figure 14.a,b), N_2-driven LACS 100W (See Figure 14.c,d), and N_2-driven LACS 200W (See Figure 14.e,f) specimens. Note that the side plane of the CS specimen shares the somewhat circular and irregularly shaped pores of the top plane. CS specimens typically have a flat, pancake-like profile in the side plane due to particle flattening upon impact. The overlapping disk-shaped particles can create horizontal pores. However, Figure 14.a and Figure 14.b show no sign of either horizontal or valley shaped pores. The irregularly-shaped pores indicate that the CS powder particles were not achieving fully flattening plastic deformation, an observation supported by examining the etched grain boundaries.

Although the overall porosity level of the LACS specimens is similar to those found in the CS specimens, the LACS specimens show a change in the pore shape and size – especially in the horizontal plane. The LACS horizontal planes (See Figure 15.c and Figure 15.e) show a

decrease in the frequency of the larger irregular pores as compared to the CS horizontal plane (See Figure 15.a). However, Figure 15.b,d,e indicate very little change in the pore shape and size in the vertical plane. It should be noted that the long pores seen in Figure 15.d and Figure 15.e are aligned along the spray build up direction, indicating the existence of inter-layer porous valleys. Examples of this directionality are marked by arrows in Figure 15.d and Figure 15.e. This may indicate that the particles are undergoing more plastic deformation in the LACS specimens, which would collapse voids in the horizontal plane but not necessarily remove inter-layer porosity.

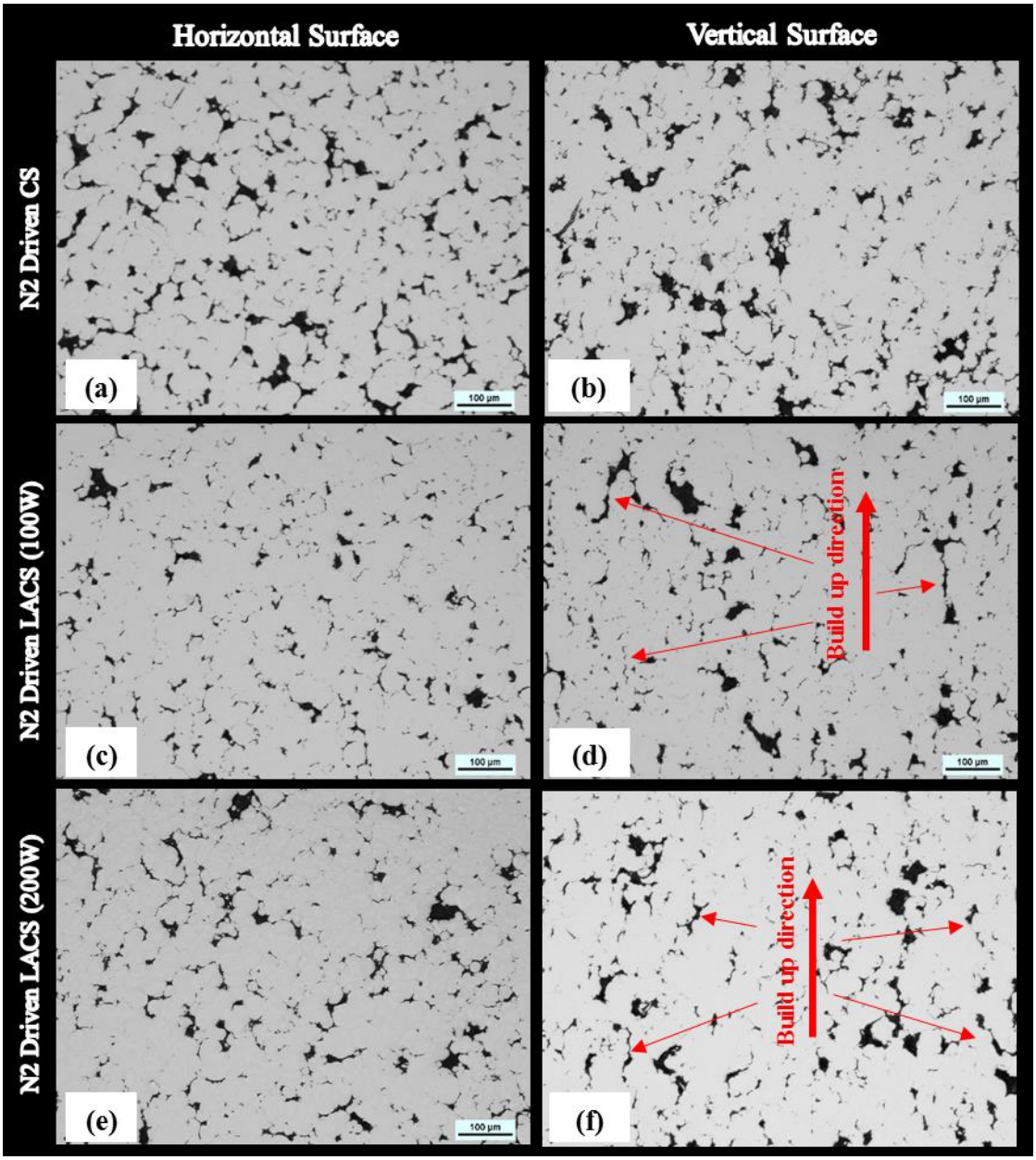

Figure 14. Porosity directionality for the (a,b) N_2-driven CS, (c,d) N_2-driven LACS 100W, and (e,f) N_2-driven LACS 200W specimens

The HIPping process drastically reduced the porosity for both the N_2-driven and the N_2 + He-driven CS specimens, which had respective area percent porosity levels of 1.5% and 0.5%. Figures 15.a,b indicate that the little porosity that does remain is more significant in the horizontal plane compared to the vertical plane. This observation is supported by Table 4, which

shows that the HIPped specimens had the greatest difference in porosity between the horizontal and vertical planes. This contrast is the result of a porosity gradient seen throughout the vertical planes of both HIPped specimens. Figure 16. includes stitched images that reveal the porosity gradients for the N_2-driven and N_2 + He-driven specimens, respectively. Note that both specimens exhibit moderate porosity near the substrate interface, low porosity in the intermediate layers, and the highest porosity near the outermost layers. Thus, the higher porosity seen in the horizontal plane of Figure 15.a is likely due to the plane being located near the outermost surface layers. This phenomenon is most likely due to the adhesion and work-hardening from the CS process. The layers near the substrate interface must overcome inter-material differences and do not as readily deform as the particles undergoing cohesion with other Ti-6Al-4V particles. Conversely, the particles near the surface of the deposition are not deformed and work-hardened by the impounding particles.

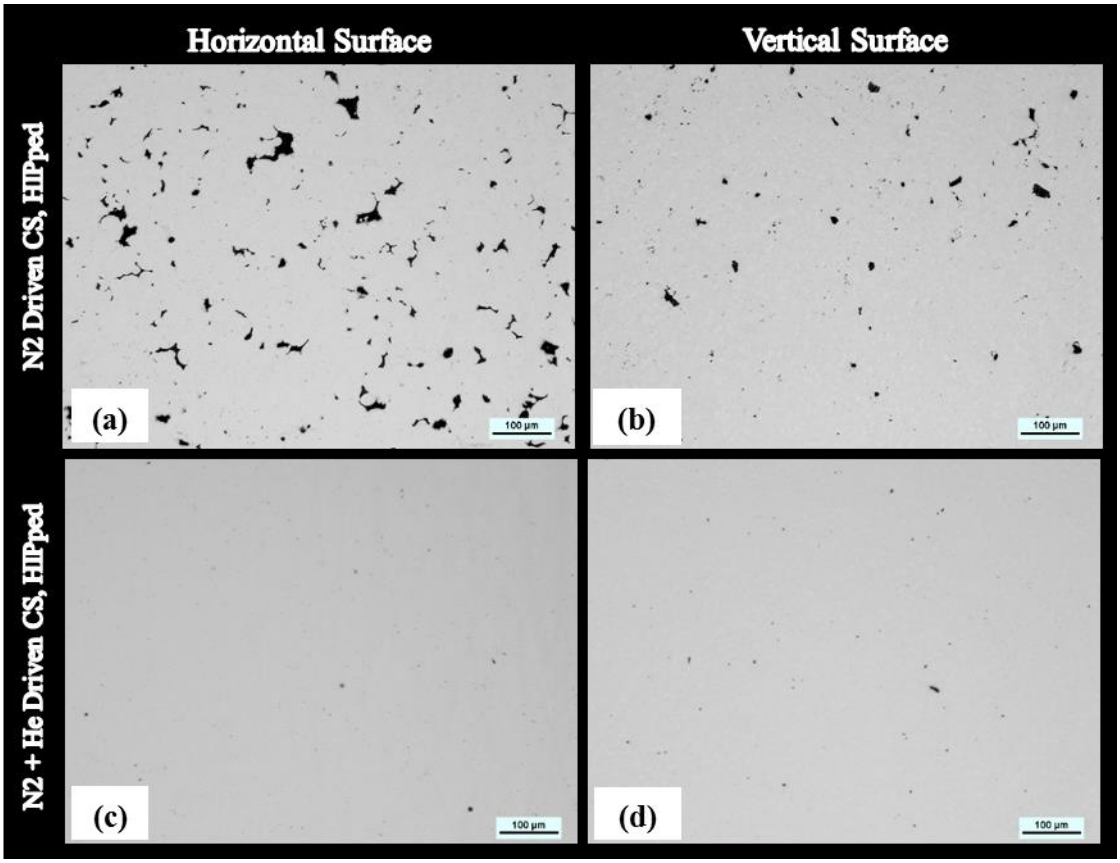

Figure 15. Porosity comparisons between the N_2-driven and the N_2 + He-driven HIPped specimens

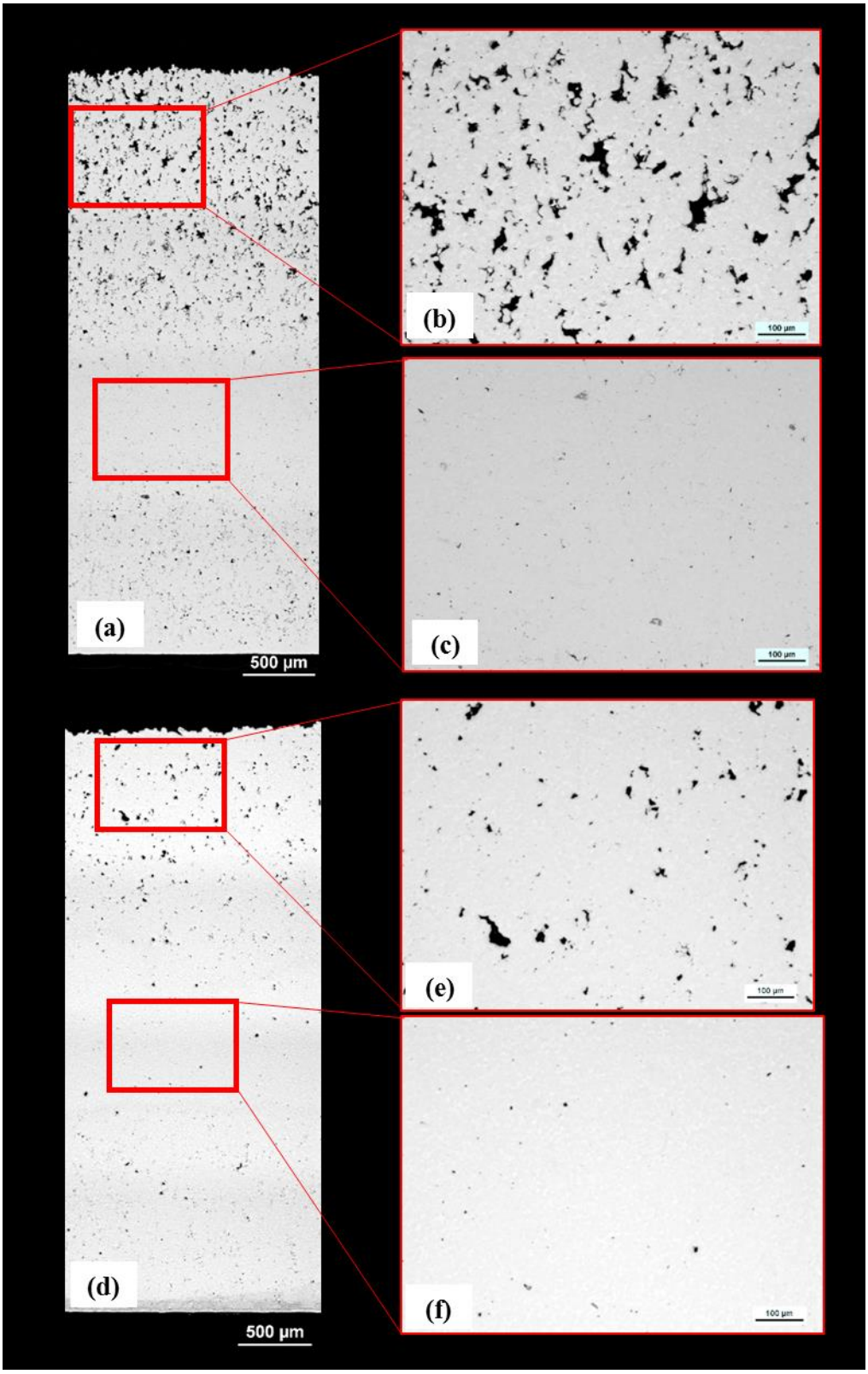

Figure 16. Porosity gradients were observed in the N_2-driven (a-c) and the N_2+He-driven (d-f) HIPped specimens

From Table 4, the He-driven CS specimen has an area percent porosity of 0.7% in the horizontal plane and 0.3% in the vertical plane, marking a substantial improvement over the N_2-driven CS specimens (See Figure 17). This reduction is an even larger improvement for the CS specimen than the HIPping process of the N_2-driven specimens, which resulted in a porosity of 3.54% in the horizontal plane and 1.59% in the vertical plane. Due to the low porosity levels in the He-driven coating, HIPping is not necessary. Indeed, the HIPped N_2+He mixture specimen has a porosity of 0.27% in the horizontal plane and 0.25% in the vertical plane, which are more porous than the as-sprayed He-driven CS specimens (See Figure 18).

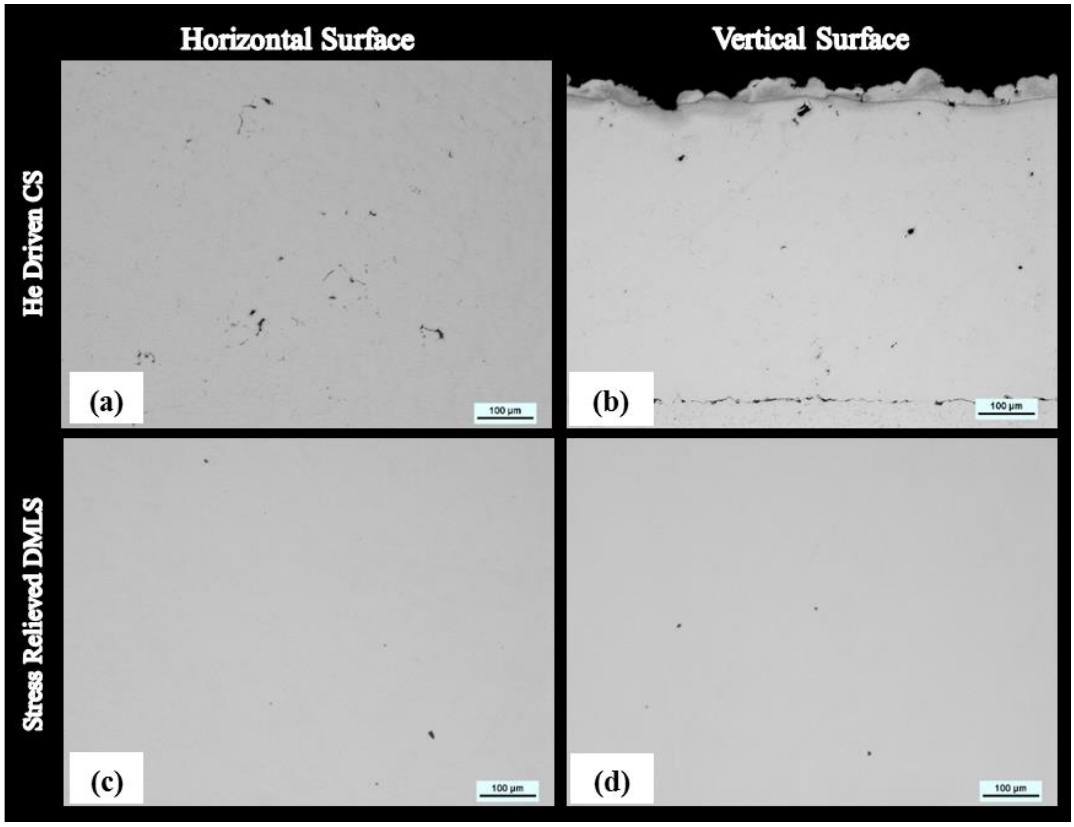

Figure 17. Porosity comparison between the He-driven CS (a-b) and the stress relieved DMLS (c-d) specimens

The stress-relieved DMLS specimen has an excellent area percent porosity of only 0.6% in the horizontal plane and 0.01% in the vertical plane. The few pores that did remain were small, isolated, and circular. This low porosity level is expected and is a benefit of DMLS's laser melting and post-process stress relief. The DMLS porosity level is significantly lower than that of the N_2-driven CS, LACS, and HIPped specimens, and similar to the porosity levels of the He-driven CS and N_2+He-driven HIPped specimens, shown in Figure 18.

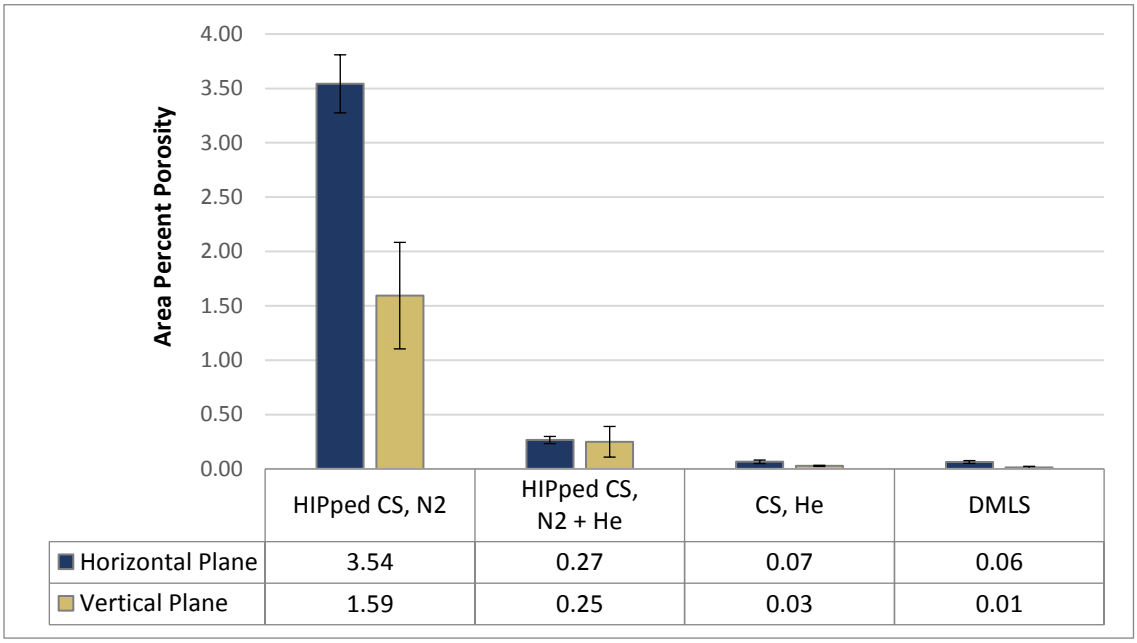

	HIPped CS, N2	HIPped CS, N2 + He	CS, He	DMLS
Horizontal Plane	3.54	0.27	0.07	0.06
Vertical Plane	1.59	0.25	0.03	0.01

Figure 18. Porosity comparison between the HIPped CS, He-driven CS, and DMLS specimens The error bars represent the SEM calculated across ten micrographs for each specimen

4.2 Microstructure

Etching revealed that specimens share a common composition of martensitic α' grains in an α-β matrix. However, the grain size, orientation, and prominence of the martensitic grains varies greatly throughout the specimens and may have a significant impact on mechanical properties. The majority of the CS and LACS as-sprayed specimens have a microstructure that closely resembles the reported microstructure of the feedstock powder [22]. This similarity is desirable and expected, as discussed earlier. Figure 19 includes a series of micrographs of the N_2-driven CS specimen in the horizontal and vertical planes and at magnifications of 100x, 500x, and 1000x. Figure 19.b,d,e provide micrographs of the particles in the vertical plane. Note that the grains have a much more circular shape in the horizontal plane (See Figure 19.d) whereas they have a much more flat plate shape in the vertical plane (See Figure 19.c), clearly indicating the deformation during the CS process. For clarity, the grain boundaries have been outlined in a dotted line in Figure 19.c and Figure 19.d. Furthermore, the presence of thin cracks along the grain boundaries suggests that the particles are not fully bonded to each other but instead underwent partial cohesion.

Within the grains, Figure 19 shows a consistent and solid foggy white composition that is indicative of an α-β matrix. At first appearance, the microstructure appears to lack the overtly distinguishing appearance of lathe-shaped martensitic α' grains. However, nucleation sites of the martensitic α' phase still exist within the grains and can be most readily identified by the thin blurred regions near the outside of the grains. The relatively subtle presence of the nucleation sites indicates that the martensitic grains began forming during atomization but were quickly cooled before being able to grow into their iconic lathe-shape. That being said, some grains do exhibit a slightly more mature martensitic phase that is evidenced by the thin and subtle lines

neighboring the particles' grain boundaries. The size and location of these grains suggest that they are the result of the localized heating from the adiabatic shear stress generated during bonding. The arrows in Figure 19.e and Figure 19.f identify example regions of small martensitic grains.

Finally, note that many of the CS and LACS micrographs include circular droplet-shaped objects along the grain boundaries. These marks are likely not due to water, lubricant, or other contaminants since specimens were ultrasonically cleaned in an ethanol bath for 10 minutes and subsequently gently airbrushed. Instead, the marks are likely due to the etchant reagent becoming entrapped in existing pores along the grain boundaries. The result is that the etchant expands the existing pores to create a collection of larger, unsightly pockets.

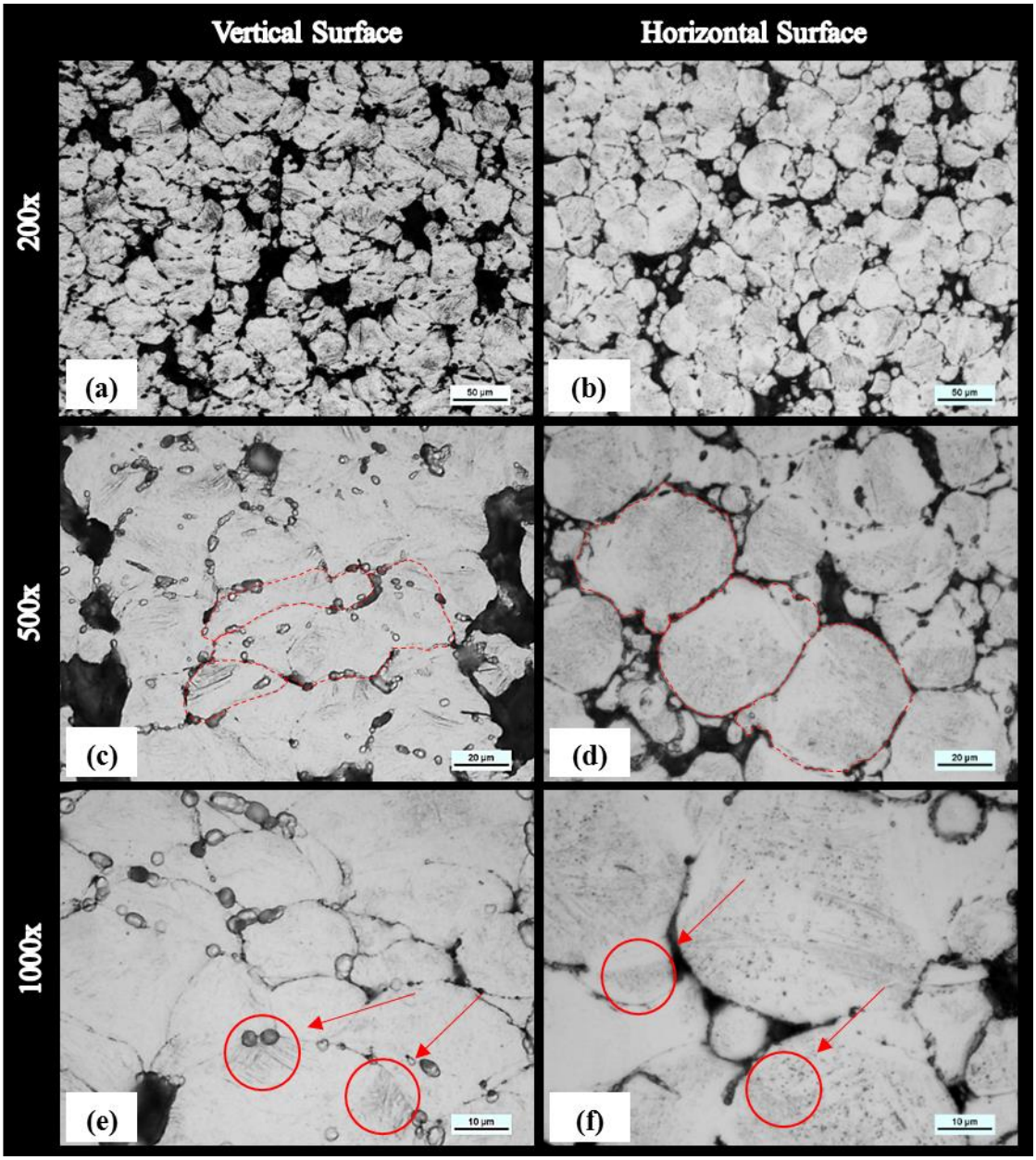

Figure 19. Microstructure of N_2-driven CS in the horizontal (a,c,e) and vertical (b,d,f) planes

The same features discussed in the N_2-driven CS specimen can be found in the N_2-driven LACS specimens and the He-driven CS specimens. The resulting micrographs are shown in Figure 20 and Figure 21. The LACS specimens' remarkably similar microstructures to the CS specimen suggest that a more aggressive laser power may be needed to affect a change. Because

damage to the microstructure does not appear to be occurring at 100W or 200W, an increase in the laser power may allow for a more drastic improvement in porosity while still maintaining a consistent microstructure with CS.

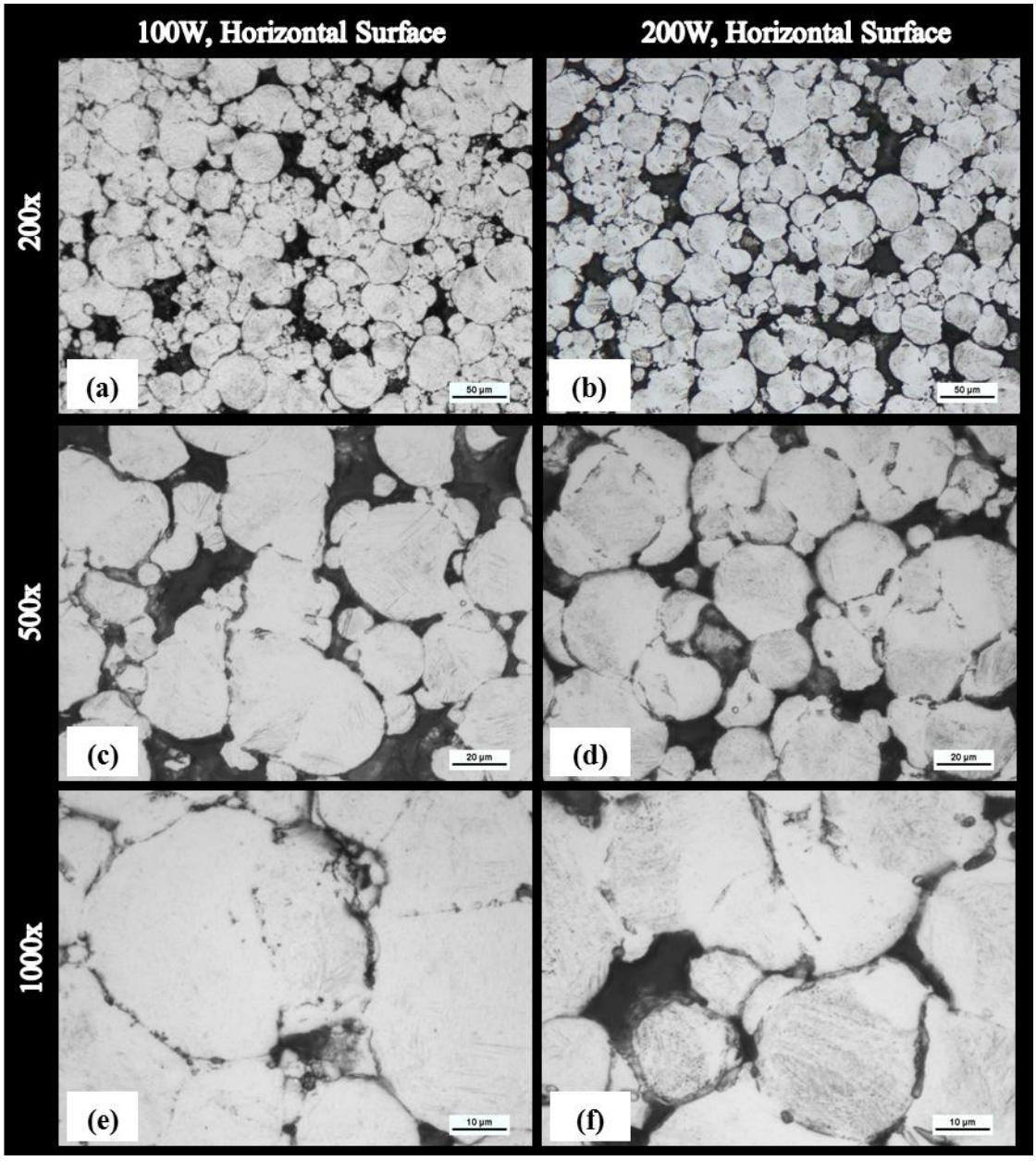

Figure 20. Microstructure of N_2-driven LACS in the horizontal planes

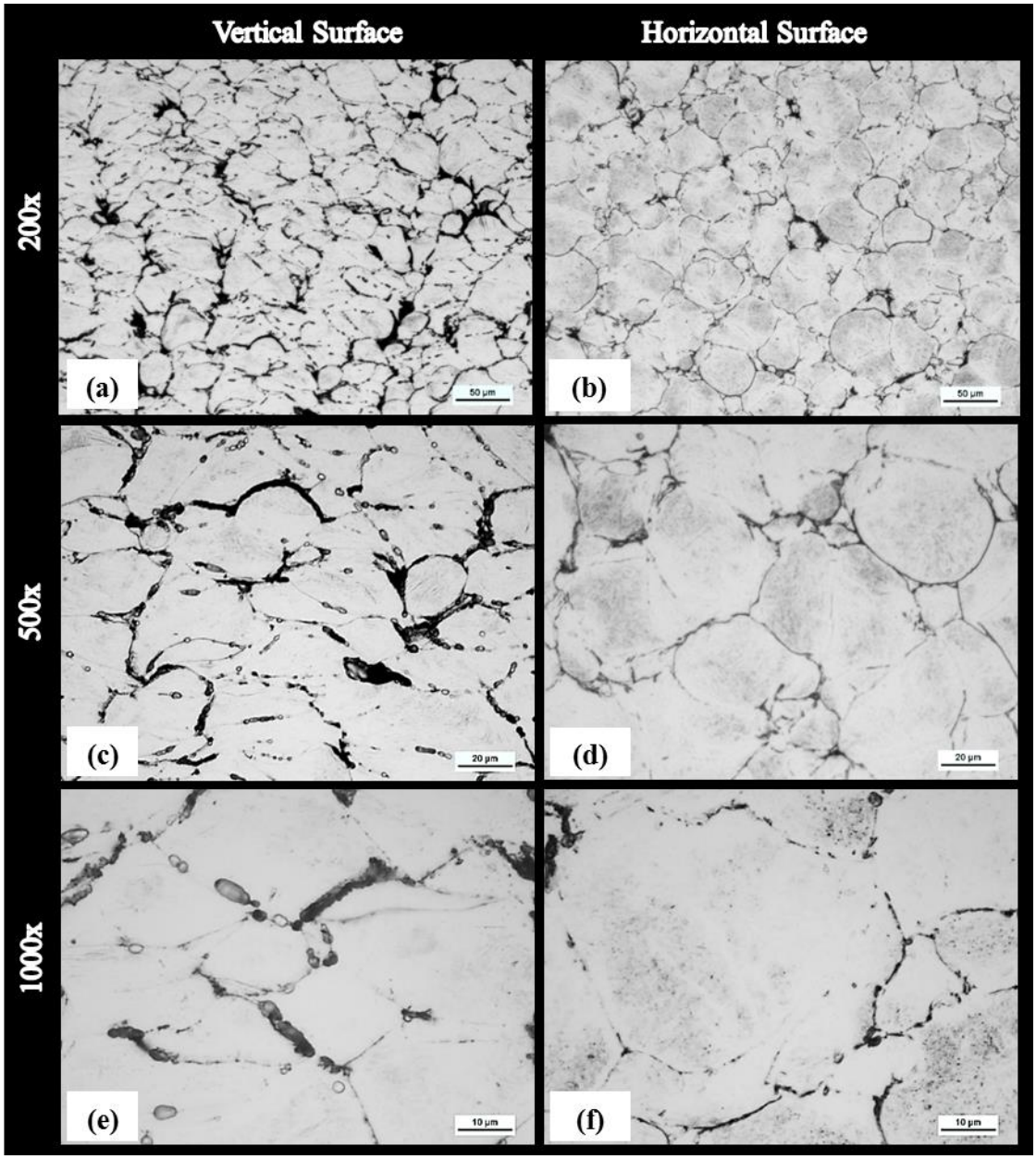

Figure 21. Microstructure of He-driven CS in the horizontal (a,c,e) and vertical (b,d,f) planes

The microstructure of the HIPped CS specimens exhibits some significant differences compared to the as-sprayed CS and LACS specimens. The principle difference is that the martensitic grains are more prominent in the HIPped specimens, as seen in Figure 22. Interestingly, the growth of the martensitic lathe grains is not consistent throughout the entirety

of the specimens, but rather it is restricted to a relatively few isolated grains. Some examples of the isolated yet pronounced martensitic phase can be found in Figure 22.c-f. This phenomenon may be due to the varying presence of existing nucleation sites throughout the grains. Also, the enclosed pores within the HIPped specimens may have acted as air reservoirs, cooling the surrounding region. However, this explanation is complicated by the martensitic regions surrounded by porosity, such as the region identified by the red arrow in Figure 22.a. It should be noted that the larger martensitic regions shown in Figure 22.e and Figure 22.f are extreme cases, and the regions were often much smaller, as shown in Figure 23.e and Figure 23.f.

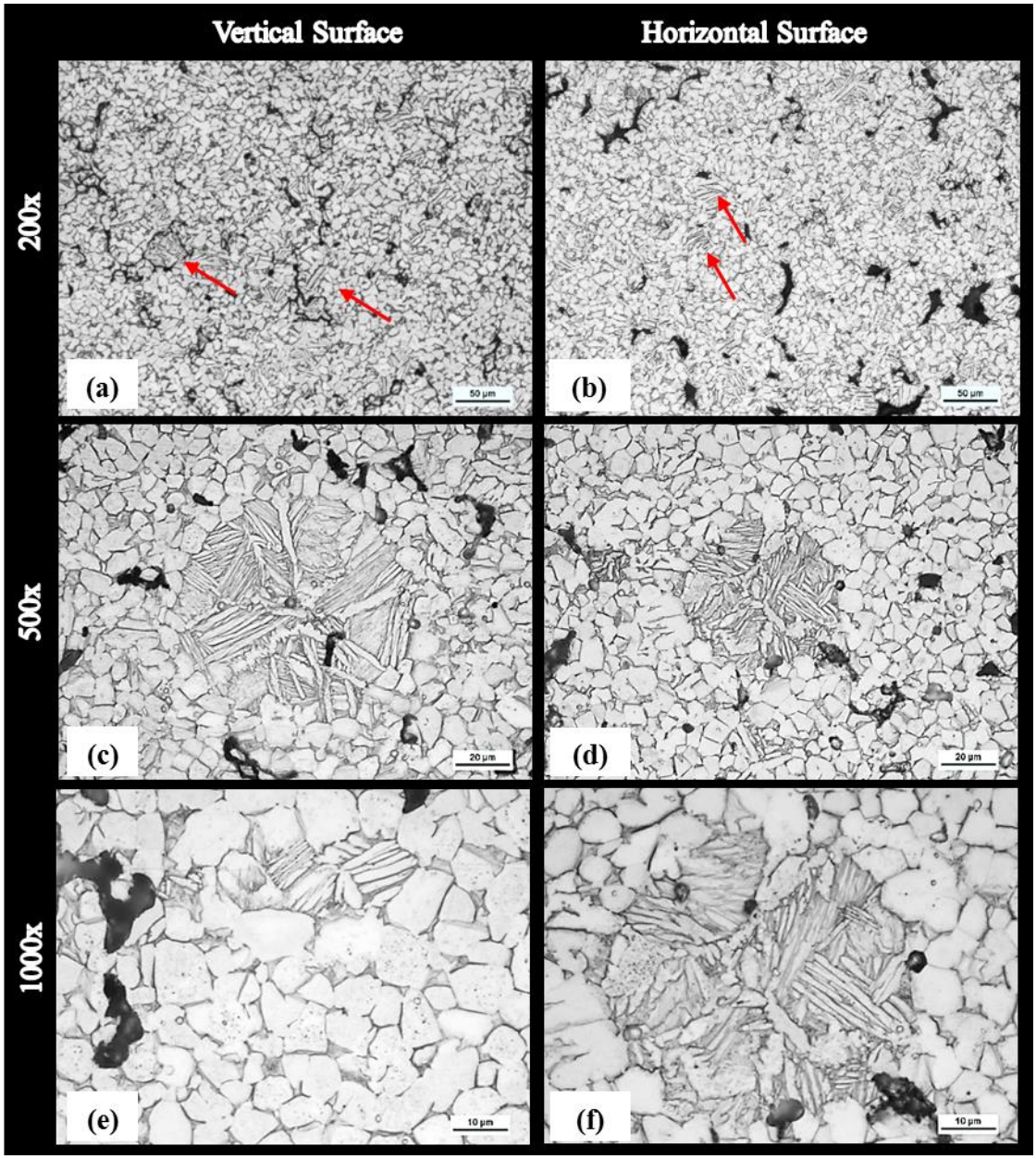

Figure 22. Microstructure of N_2-driven HIPped CS in the horizontal (a,c,e) and vertical (b,d,f) planes

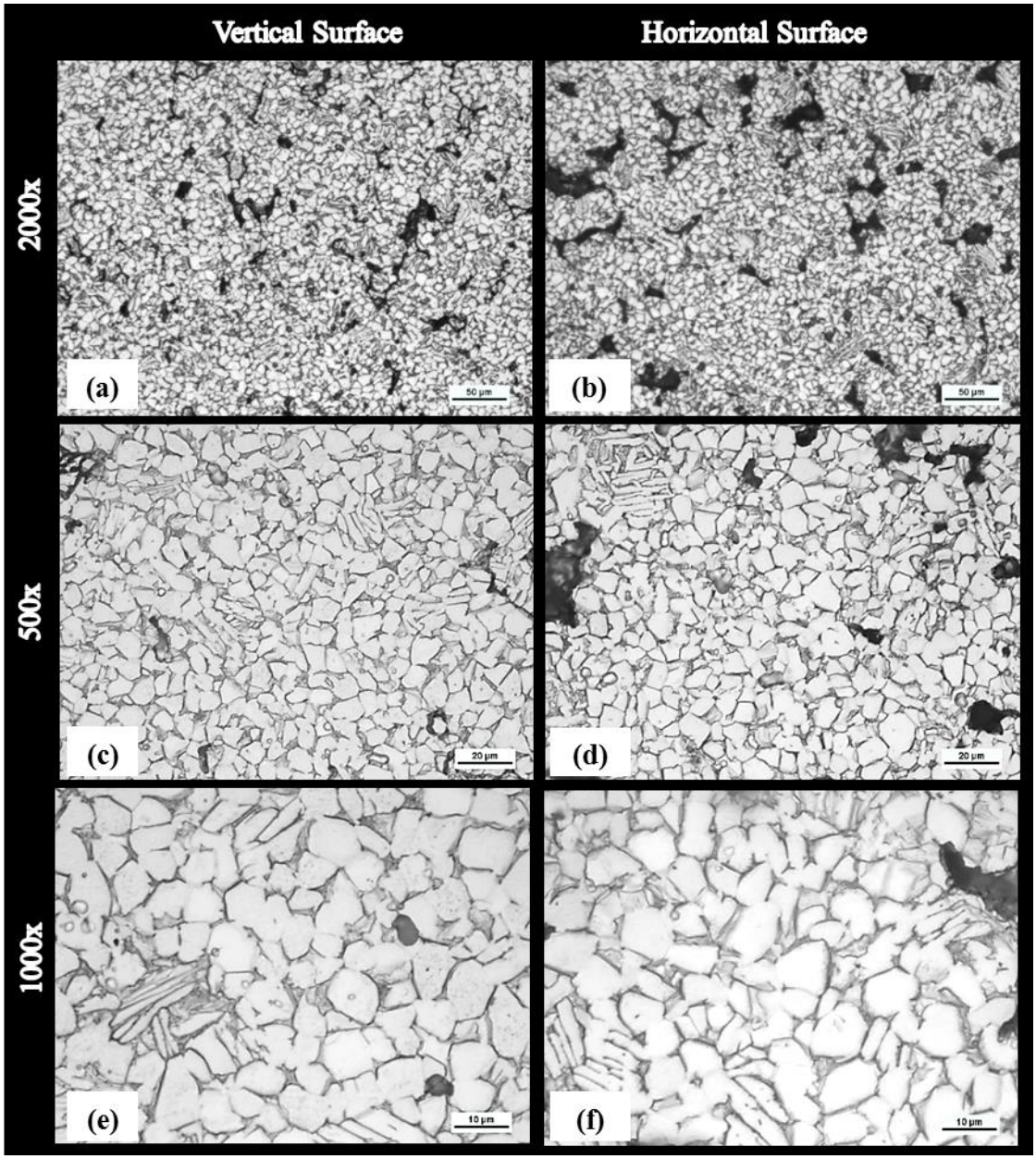

Figure 23. Microstructure of He + N_2-driven HIPped CS in the horizontal (a,c,e) and vertical (b,d,f) planes

It is interesting to note that the HIPped specimens had excellent adhesion to the steel substrate, as shown in Figure 24. This may be because the steel readily underwent adiabatic shear stress and mechanical interlocking, creating a stronger bond near the material interface.

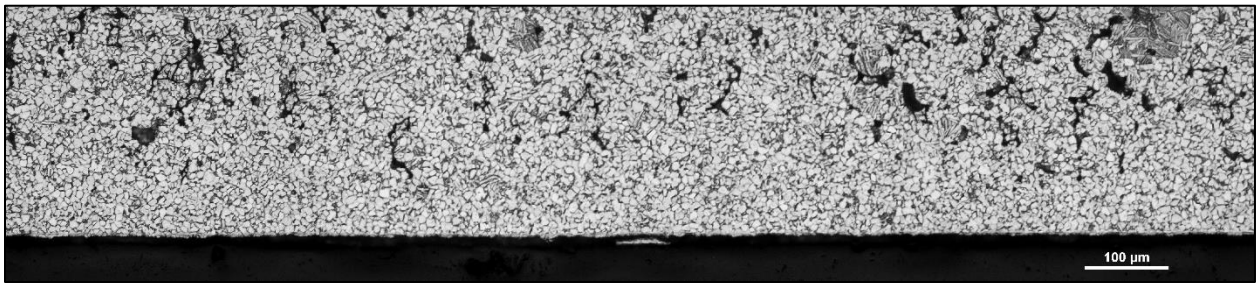

Figure 24. The Hipped CS specimens exhibited excellent adhesion to the steel substrate

Finally, the DMLS specimen exhibited a drastically different microstructure compared to the CS and LACS specimens. Even in the most extreme cases, the CS and LACS specimens had sporadic and isolated cases of martensitic growth. Conversely, in the DMLS specimen, the martensitic growth is dominant and spreads throughout the entirety of the grains. From Figure 25, the lathes can be seen to be continuous, longer and perpendicular to each other – common features of fully grown martensitic α grains.

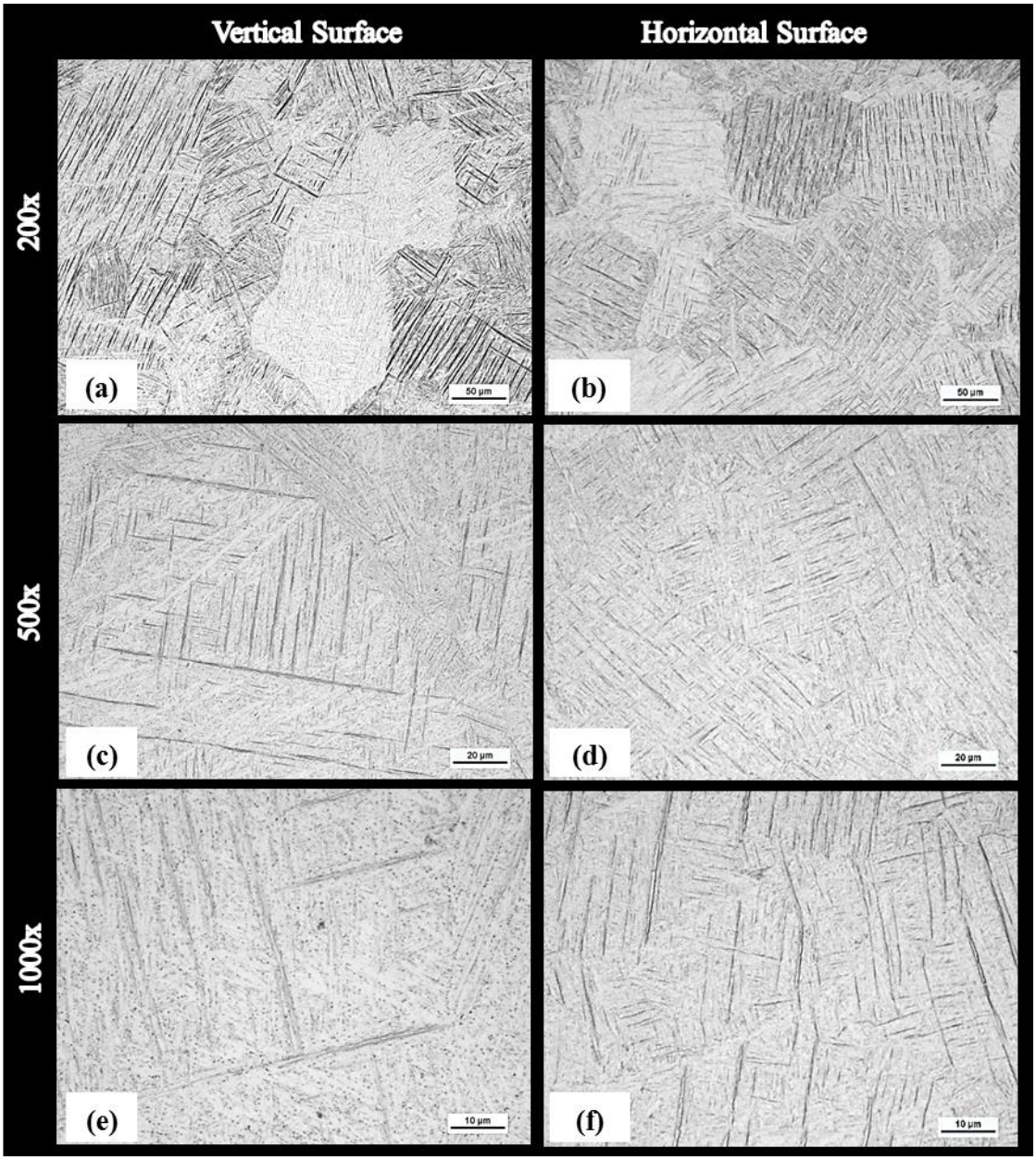

Figure 25. Microstructure of DMLS in the horizontal (a,c,e) and vertical (b,d,f) planes

4.3 Microhardness

All of the tested specimens exhibited a Vickers hardness value within the expected range of values. Still, several key differences were observed among the specimens. A comparison of the VHN values are summarized in Figure 26. Figure 26 displays the average of 20 VHN indentations on the horizontal plane and includes the standard error of the mean (SEM) for each specimen. Among the N_2-driven CS and LACS specimens, average microhardness is consistent. That is, the CS, LACS at 100W, and LACS at 200W specimens have a respective average hardness of 380 VHN, 378 VHN, and 383 VHN and a respective SEM of 5.1, 5.9, and 4.8. A t-test performed on the VHN values show a two-tailed p-value of 0.7990 and 0.6708 for the LACS specimens at 100W and 200W, respectively. These values are fair above the threshold for statistical significance. Note that porosity is influencing the microhardness data for the N_2-driven CS and LACS; although porosity was avoided when possible, nearby pores can still decrease the recorded microhardness below what would otherwise be expected.

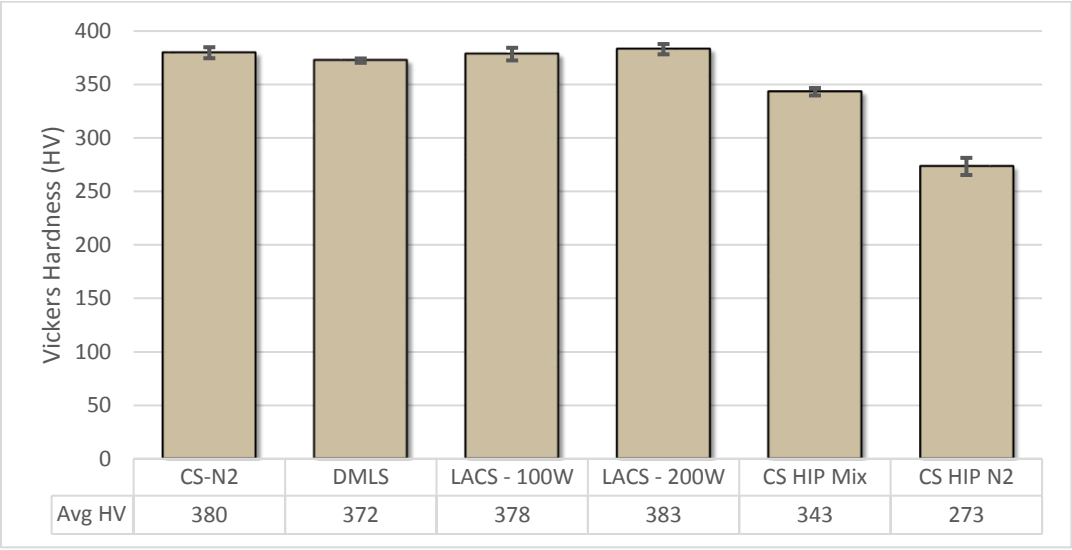

Figure 26. Microhardness summary of the tested specimens

The HIPped specimens have a significantly lower hardness than the as-sprayed CS and LACS specimens. Specifically, the N_2 + He-driven and the N_2-driven specimens have an average hardness of 343 VHN and 273 VHN and a respective SEM of 4.8 and 3.4. This decrease is likely due to the grain growth the specimens undergo during the HIPping process, which results in easier energy dispersion and more ductile behavior. The higher hardness in the N_2+He-driven HIPped specimen compared to the N_2-driven HIPped specimen is likely the result of the helium in the carrier gas resulting in a higher particle velocity, thus magnifying the work-hardening phenomenon that the deposition undergoes during CS.

The DMLS specimen has a hardness of 372 VHN with an SEM of only 2.0. This SEM is significantly smaller than the CS and LACS specimens and is likely due to the porosity in the CS and LACS specimens introducing variations between the indentation sites. Even within the bounds of the SEM, the CS and LACS specimens exhibit a slightly higher hardness compared to the DMLS specimen. The increased hardness in the CS and LACS specimens is likely the combined effect of particle impact work-hardening in the sprayed specimens and heat relieving in the DMLS specimen. Note that the average hardness of wrought Ti-6Al-4V is approximately 360 VHN [36]. Thus, the as-sprayed CS and LACS and the stress relieved DMLS specimens all exhibited a higher microhardness than wrought Ti-6Al-4V. This is likely the result of work hardening in the CS and LACS specimens and severe heating and cooling in the DMLS specimen.

Table 5. Summary of average Vicker's microhardness data

	N_2-Driven CS	N_2-Driven LACS (100W)	N_2-Driven LACS (200W)	N_2-Driven CS, HIPped	N_2 + He-Driven CS, HIPped	DMLS
Avg VH	380	378	383	273	343	372
SEM	5.1	5.9	4.8	8.0	3.4	2.0
SD	22.4	25.7	21.0	35.0	15.0	8.8

All specimens exhibited a very slight decrease in hardness in the vertical plane compared to the horizontal plane. The CS specimen dropped 14 VHN on average from 380 to 366 VHN, and the LACS specimen dropped 19 VHN on average from 378 to 359 VHN. The DMLS specimen had the smallest directionality, dropping 7 VHN on average from 372 VHN to 365 VHN. The decreased transverse hardness in the CS and LACS specimens indicates that there may be a directionality to the work hardening behavior within the coating. The 7 VHN difference between the orientations of the DMLS specimens is within the range of one standard deviation and is unlikely to be indicative of any microstructural variation.

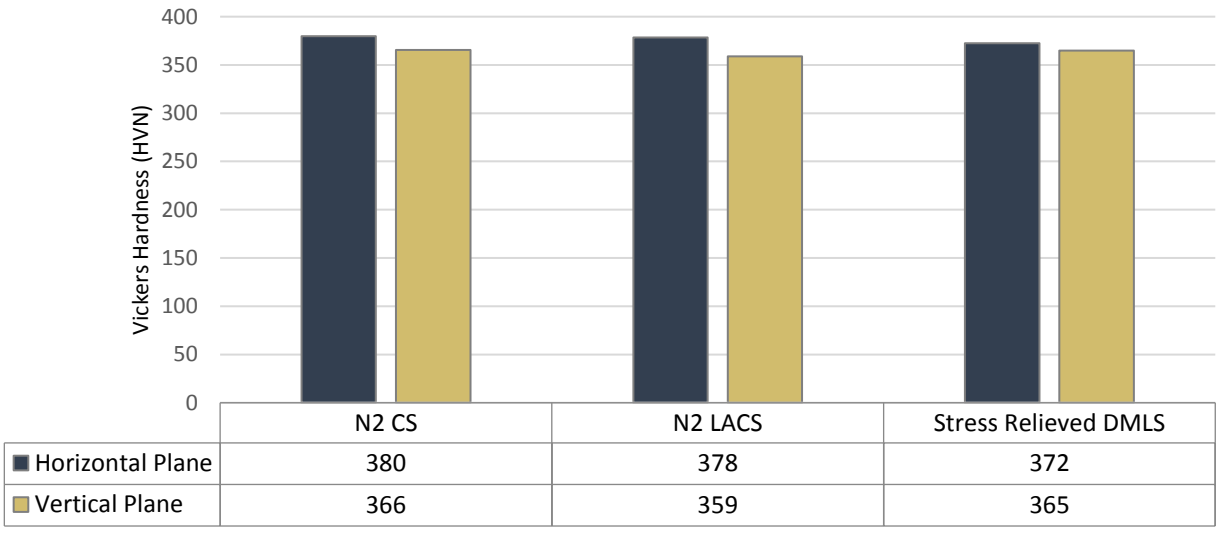

Figure 27. Microhardness sensitivity to orientation

4.4 Summary of Results

The results reveal very similar porosity levels, microstructure, and microhardness between the parts fabricated from CS and LACS. However, a significant decrease in porosity was achieved when using helium as the MPG. Microstructure was consistent regardless of the MPG. Also, HIPping the CS specimens significantly decreased porosity, but also decreased the microhardness. Interestingly, the as-sprayed He-driven CS specimens exhibited lower porosity than the HIPped N_2-driven CS, indicating that using helium as the MPG selection may influence porosity even more than the HIPping process. The HIPped N_2+He-driven CS specimens had the lowest porosity, a microstructure consistent with the as-sprayed CS and LACS specimens, and intermediate microhardness. In all scenarios, the microstructures of the CS and LACS fabricated specimens resembled the reported microstructure of the feedstock powder. The DMLS fabricated specimen exhibited the lowest porosity, and its microstructure was dominated by α' martensitic lathe-shaped grains. The DMLS fabricated specimen had a microhardness comparable to the as-sprayed CS and LACS specimens. The CS, LACS, and DMLS specimens all exhibited higher microhardness than commonly reported values for wrought Ti-6Al-4V.

Chapter 5

Conclusions and Future Work

5.1 Conclusions

Several conclusions can be drawn with respect to the porosity, microstructure, and microhardness of the CS, LACS, and DMLS specimens. A summary of these conclusions follow.

Porosity:

- The CS and LACS specimens exhibited porosity levels between 9.05% - 9.62%. This is in agreement with previous findings, which range from 8.9% to 22.3%.
- LACS of Ti-6Al-4V with laser powers of 100W and 200W show minimum improvement in porosity compared to CS of Ti-6Al-4V ($t(18)=1.79$, $p = 0.0899$)
- Increasing the laser power may further decrease the porosity in LACS of Ti-6Al-4V.
- Replacement of helium for nitrogen as the driving gas results in an extremely statistically significant reduction in porosity in the CS specimens ($t(18)=17.35$, $p < 0.0001$).
- The HIPping process significantly reduced the porosity compared to the as-sprayed CS and LACS specimens ($t(18)=11.0304$, $p < 0.0001$). A MPG mixture of helium and nitrogen provide further statically significant decrease in porosity($t(18)=12.1423$, $p < 0$). However, the specimens exhibit a limiting porosity level of approximately 0.5%.
- The heat-relieved DMLS specimen shows extremely low levels of porosity in both the transversal (0.06% area) and longitudinal (0.01% area) directions.

Microstructure:

- Microstructure of the CS and LACS specimens closely resembles that of the feedstock powder, namely, small isolated pockets of early martensitic α' and nucleation sites of martensitic α' within an α-β matrix.
- Microstructure of the DMLS specimen is dominated by large, lathe-shaped martensitic α' phases that fully transverse the grains.
- Microstructure of the Ti-6Al-4V LACS is indistinguishable from the Ti-6Al-4V CS, and there are no signs of thermal effects from the heating laser. Because thermal effects are not evident at 100W and 200W, it may be possible to increase laser power to improve porosity whilst still avoiding thermal effects in the microstructure.
- HIPping did not significantly affect the microstructure of the CS and LACS specimens except for the formation of isolated pockets of lathe-like martensitic α'.

Vickers Microhardness:

- There is no statistically significant difference between the Ti-6Al-4V CS and LACS specimens (Horizontal: $t(38)=0.26$, $p = 0.7990$) (Transverse: $t(38)=0.71$, $p = 0.4851$).
- The CS and LACS specimens have a slightly higher VHN value in the longitudinal direction compared to the transverse direction ($t(38)=2.04$, $p = 0.0485$). This may be due to the longitudinal work-hardening observed in the CS process.
- The CS and LACS Ti-6Al-4V specimens exhibited a wider spread in HVN values compared to the DMLS specimen (SEM values of 5.1 and 5.9 versus 2.0). The spread is likely the influence of porosity neighboring the indentation sites.

- The CS, LACS, and DMLS specimens all exhibited higher microhardness than commonly reported values for wrought Ti-6Al-4V. The higher hardness may be the result of work hardening in the CS, and LACS specimens and severe heating and cooling in the DMLS specimen.
- The HIPping process significantly decreases the hardness of the CS and LACS Ti-6Al-4V specimens.
- All specimens showed a decrease in hardness in the transverse direction compared to the longitudinal direction.

5.2 Limitations and Future Work

Although this thesis provides a valuable comparison between CS, LACS, and DMLS parts with Ti-6Al-4V, it is important to note the limitations of the study. Perhaps most importantly, the CS and LACS specimens were sprayed at three different sites, WPI, MOOG, and ARL. Although this collaboration allowed for a diverse range of technologies, it introduced a level of inherent uncertainty due to unaccountable differences between systems. Furthermore, the feedstock powder for the DMLS specimen was not from the same batch or manufacturer as the feedstock powder for the CS and LACS specimens. Efforts were made to obtain as similar of powder as possible, but particle size distribution (PSD) and microstructure differences in the feedstock powder may influence the porosity and microstructure of the final part. Finally, the LACS specimens used relatively conservative powers of 100W and 200W. These powers were selected to show the introductory efforts of laser heating in CS, but a larger laser power would likely result in a more significant difference between the CS and LACS specimens.

This investigation serves as the groundwork for potential future research into the mechanical properties of CS, LACS, and DMLS of Ti-6Al-4V. In particular, tensile test data for CS and LACS of Ti-6Al-4V is currently lacking in the literature, and several partners in this research have already expressed interest in pursuing such a study in the future. By better understanding the mechanical properties of CS, LACS, and DMLS, near net fabrication of Ti-6Al-4V may take one step closer to achieving large scale industrial adoption.

APPENDIX A

Optical Microscopy Porosity Data

Micrograph Site Number	CS, N2	LACS (100W)	LACS (200W)	HIPped CS, N2	HIPped CS, N2 + He	CS, He	DMLS
	Horizontal Plane (Longitudinal)						
1	8.17	11.42	10.32	1.43	0.45	0.02	0.04
2	9.74	12.06	8.11	3.34	0.32	0.13	0.03
3	9.38	7.03	9.75	3.65	0.23	0.01	0.14
4	11.17	9.36	8.71	3.87	0.13	0.05	0.12
5	9.01	9.99	12.58	3.08	0.19	0.05	0.09
6	8.93	7.35	11.35	3.77	0.39	0.02	0.06
7	11.80	11.35	6.75	4.55	0.22	0.07	0.09
8	13.93	7.93	8.79	2.52	0.34	0.16	0.11
9	11.28	6.69	9.43	3.40	0.19	0.01	0.04
10	13.22	7.59	7.31	3.47	0.19	0.06	0.03
	Vertical Plane (Longitudinal)						
1	7.62	13.27	10.72	4.30	0.19	0.04	0.02
2	9.57	12.34	9.62	3.30	0.08	0.02	0.03
3	10.33	9.01	6.65	4.38	0.10	0.05	0.00
4	9.87	0.48	5.42	4.96	0.34	0.00	0.08
5	10.72	8.83	3.71	4.05	0.23	0.00	0.09
6	8.93	10.99	13.28	0.59	0.54	0.01	0.06
7	11.39	10.15	8.58	1.84	0.24	0.01	0.04
8	10.41	9.20	7.78	0.86	0.23	0.02	0.00
9	8.71	9.73	8.35	1.84	0.19	0.02	0.01
10	10.54	9.24	7.81	2.84	0.30	0.01	0.03

APPENDIX B

Vickers Microhardness Indentation Data

Indentation Site Number	Horizontal Plane (Longitudinal)					Vertical Plane (Transversal)		
	CS	LACS (100W)	LACS (200W)	HIPped CS, N2	HIPped CS, N2 + He	DMLS	CS	LACS (100W)	DMLS
1	389	363	338	262	345	360	346	354	367
2	361	336	390	220	344	375	332	351	363
3	412	314	397	242	377	365	393	372	356
4	370	355	356	275	379	353	337	393	355
5	364	383	343	307	350	376	386	331	365
6	407	374	358	315	356	389	366	394	361
7	396	416	408	260	346	380	378	308	367
8	347	360	383	318	332	381	382	402	371
9	361	380	406	325	349	371	375	369	376
10	332	408	388	315	326	375	356	275	359
11	414	403	385	232	342	373	334	396	366
12	381	402	406	304	324	365	386	358	374
13	357	377	387	305	340	372	381	387	366
14	373	406	377	227	332	377	347	291	370
15	390	397	392	297	318	371	379	391	358
16	400	392	366	281	328	384	382	300	362
17	397	351	419	262	344	382	335	380	357
18	406	375	397	216	344	358	369	406	379
19	375	403	381	239	349	368	362	375	363
20	363	374	384	266	340	372	386	342	361
avg	380	378	383	273	343	372	366	359	365
SEM	5.1	5.9	4.8	8.0	3.4	2.0	4.6	8.8	1.5
SD, σ	22.4	25.7	21.0	35.0	15.0	8.8	19.9	38.4	6.5

BIBLIOGRAPHY

[1] R. Boyer, G. Welsch, and E. W. Colling, "Materials Properties Handbook: Titanium Alloys." ASM International. 1994.

[2] C. Leyens and M. Peters, "Titanium and Titanium Alloys: Fundamentals and Applications." Wiley-VCH GmbH & Co. KGaA. 2003.

[3] S. Thompson, L. Bian, N. Shamsaei, A. Yadollahi, "An Overview of Direct Laser Deposition for Additive Manufacturing; Part I: Transport Phenomena, Modeling and Diagnostics." *Additive Manufacturing*. Vol 8. pp. 36-62. Oct. 2015.

[4] V. K. Champagne, "The Cold Spray Materials Deposition Process: Fundamentals and Applications." Elsevier. 2007.

[5] A. M. Birt, V. K. Champagne, R. D. Sisson, and D. Apelian, "Microstructural Analysis of Cold-Sprayed Ti-6Al-4V at the Micro- and Nano-Scale. *Journal of Thermal Spray Technology*. vol. 24, no. 7, pp. 1277-1288. Oct. 2015

[6] H. R. Zschommler, B. V. Morante, and P. A. Suzuki, "Kinetics of thermal decomposition of titanium hydride powder using in situ high-temperature X-ray diffraction." Materials Research. vol. 8, no. 3, pp. 293-297. Sept. 2005

[7] M. J. Donachie, "Titanium: A Technical Guide." *ASM International*. Heat Treating Titanium and its Alloys." Second Edition. Ch. 8, pp. 381. Dec. 2000.

[8] A. Papyrin, V. Kosarev, and S. Klinkov, "Cold Spray Technology." *Elsevier's Science and Technology*. First Edition. 2007.

[9] M. Grujicic, W. S. DeRosset, and D. Helfritch, "Flow analysis and nozzle-shape optimization for the cold-gas dynamic-spray process." *Proceedings of the Institution of*

Mechanical Engineers. Part. B: Journal of Engineering Manufacture. vol. 217, no. 11, pp. 1603-1313. Nov. 2003.

[10] D. I. Adebiyi, I. Botef, and P. Popoola, "Computational technique for optimization of the process parameter for cold spray coating of titanium." Proceedings of the 1st International Conference on Mathematical Methods & Computational Techniques in Science & Engineering. pp. 28-30. Nov. 2014.

[11] H. Singh, T. Sidhu, and S. Kalsi, "Cold Spray Technology: Future of Coating Deposition Processes" Frattura ed Integrita Strutturale. vol. 22. pp. 69-84. 2012.

[12] K. Balani, T. Laha, A. Agarwal, J. Karthikeyan, and N. Munroe, "Effect of carrier gases on microstructural and electrochemical behavior of cold-sprayed 1100 aluminum coating." *Surface & Coating Technology*. vol. 195, pp. 272-279. 2005.

[13] S. Yin, X. Suo, H. Liao, Z. Guo, and X. Wang, "Significant influence of carrier gas temperature during the cold spray process." *Surface Engineering*. vol. 30, no. 6, pp. 443-450. June 2014.

[14] M. Gruijicic, C. Zhao, C. Tong, W. DeRosset, and D. Helfritch, "Analysis of the impact velocity of powder particles in the cold-gas dynamic-spray process." *Materials Science and Engineering*. vol. A368, pp. 222-230. 2004.

[15] W. Li, D. G. Liao, and C. Coddet, "Optimal Design of a Cold Spray Nozzle by Numerical Analysis of Particle Velocity and Experimental Validation with 316L Stainless Steel Powder." *Materials and Design*. vol. 28, pp. 2129-2137. 2007.

[16] A. Alexeenko, D. Levin, S. Gimelshein, R. Collins, and B. Reed, "Numerical Modeling of Axisymmetric and Three-Dimensional Flows in Microelectromechanical Systems

Nozzles." *American Institute of Aeronautics and Astronautics.* vol. 40, no. 5, pp. 897-904. May 2002.

[17] M. Ur Rab, S. Zahiri, S. Masood, M. Jahedi, and R. Nagarajah, "Development of 3D Multicomponent Model for Cold Spray Process Using Nitrogen and Air." *Coatings: Trends in Coatings and Surface Technology.* Vol. 5, pp. 688-708. Oct. 2015.

[18] M. Tlotleng, E. Akinlabi, Ml. Shukla, S. Pityana, "Application of Laser Assisted Cold Spraying Process for Materials Deposition" Published in Surface Engineering Techniques and Applications: Research Advancements. pp. 177-221. Feb. 2014.

[19] M. Bray, A. Cockburn, W. O'Neill, "The Laser-assisted Cold Spray process and deposit characterization." *Surface and Coatings Technology*. Vol. 203., Issue 19, pp. 2851-2857, June 2009.

[20] D. Christoulis, C. "Sarafoglou, "Modern Cold Spray." Springer International Publishing. Switzerland. Chapter 7: Laser-Assisted Cold Spray. pp. 275-302. 2015.

[21] A. Birt, V. Champagne, R. Sisson, D. Apelian, "Microstructural analysis of Ti–6Al–4V powder for cold gas dynamic spray applications." Advanced Powder Technology. Vol. 26, Issue 5, pp. 1335-1347. Sept. 2015.

[22] K. Zhang, J. Mei, N. Wain, X. Wu, "Effect of Hot-Isostatic-Pressing Parameters on the Microstructure and Properties of Powder Ti-6Al-4V Hot-Isostatically-Pressed Samples." *Metallurgical and Materials Transactions* Vol. 41, Issue 4, pp. 1033-1045, April 2010

[23] A. Birt, V. Champagne, R. Sisson, D. Apelian, "Microstructural Analysis of Cold-Sprayed Ti-6Al-4V at the Micro- and Nano-Scale." *Journal of Thermal Spray Technology*. Vol. 24, Issue 7, pp. 1277-1288, Oct. 2015

[24] C. Moy, J. Cairney, G. Ranzi, M. Jahedi, S. Ringer, "Investigating the microstructure and composition of cold gas-dynamic spray (CGDS) Ti powder deposited on Al 6063 substrate." *Surface and Coatings Technology*. Vol. 204, Issue 23, pp. 3739-3749. Aug. 2010

[25] D. Rafaja, T. Schucknecht, V. Klemm, A. Paul, "Microstructural characterisation of titanium coatings deposited using cold gas spraying on Al2O3 substrates." *Surface and Coatings Technology.* Vol 203, Issues 20-21. pp. 3206-3213. July 2009

[26] W. Li, C. Zhang, X. Guo, J. Xu, C. Li, H. Liao, C. Coddet, K. Khor, "Ti and Ti-6Al-4V Coatings by Cold Spraying and Microstructure Modification by Heat Treatment." Advanced Engineering Materials. Vol. 9. Issue 5. pp. 418-423. May 2007.

[27] M. Khaing, J. Fuh, L. Lu. "Direct metal laser sintering for rapid tooling: processing and characterisation of EOS parts." *Journal of Materials Processing Technology.* Vol. 113, Issues 1-3. pp. 269-272. June 2001.

[28] L. Bertol, W. Junior, F. Pinto da Silva, C. Aumund-Kopp, "Medical design: Direct metal laser sintering of Ti–6Al–4V." *Materials & Design*. Vol. 31. Issue 8. pp. 3982-3988. Sept. 2010

[29] L. Murr, S. Gaytan, D. Ramirez, E. Martinez, J. Hernandez, K. Amato, P. Shindo, F. Medina, R. Wicker, "Metal Fabrication by Additive Manufacturing Using Laser and Electron Beam Melting Technologies." Journal of Materials Science & Technology. Vol. 28, Issue 1. pp. 1-14. Jan. 2012.

[30] M. Simonelli, Y. Tse, C. Tuck, "Further Understanding of Ti-6Al-4v Selective Laser Melting Using Texture Analysis." *Solid Freeform Fabrication Proceedings.* Annual international solid freeform fabrication symposium. pp. 480-491. 2012.

[31] M. Khaing, J. Fuh, L. Lu, “Direct metal laser sintering for rapid tooling: processing and characterisation of EOS parts.” *Journal of Materials Processing Technology*. Vol. 113, Issues 1-3. pp. 269-272. June 2001.

[32] Advanced Powders & Coatings. “Titanium alloy powder: Ti-6AI-4V.” Advanced Powders and Coatings Inc. Web. 2014. advancedpowders.com/our-plasma-atomized-powders/products/ti-6al-4v-titanium-alloy-powder/#15-45_m

[33] G. F. Voort, “Titanium Specimen Preparation” *Advanced Materials & Processes*. Vol. 167, Issue 2, pp. 25-27. Feb. 2008.

[34] B. Taylor, E. Weidmann, “Metallographic preparation of titanium.” Struers Application Note 02.2016 / 62140202. 2015. pp. 1-6.

[35] T. Hussain, “Cold Spraying of Titanium: A Review of Bonding Mechanisms, Microstructure and Properties.” *Key Engineering Materials.* Vol. 533, pp. 53-90. 2013.

[36] M. Shunmugavel, A. Polishetty, G. Littlefair, “Microstructure and mechanical properties of wrought and additive manufactured Ti-6Al-4V cylindrical bars.” *Procedia Technology*. pp. 231-236. 2015.

MICHAEL J. TROWBRIDGE

394 Gregory Lane, Bellefonte, PA 16823 | mjt5370@psu.edu | (814)360-5504

EDUCATION

The Pennsylvania State University, University Park, PA — Graduating May, 2017
Bachelor of Science in Mechanical Engineering, Honors
Bachelor of Science in Engineering Science, Honors
Engineering Mechanics (minor)

- Class of 2017 Student Marshal for the Engineering Science program
- Cumulative GPA: 4.00
- Enrolled in the Penn State Schreyer Honors College
- Research: Material testing and characterization for design applications.

PROFESSIONAL EXPERIENCE

Structural Analysis Engineer — May 2016 – Present (Academic Leave of Absence)
The Boeing Company | Phantom Works — Ridley Park, PA

- Performed research and development for the CH-47 Chinook and proprietary programs
- Designed structures and components, utilizing Catia and composite design
- Outlined experimental testing of high-energy absorbing materials for crash worthiness
- Researched self-locking mechanisms for electrical connector design
- Conducted off-site mechanical testing and validation of prototype components
- Presented results and recommendations to top-level program management
- Assisted in aircraft survivability analysis
- Authored engineering orientation packet to improve efficiency of the onboarding process

Researcher - Distinguished Undergraduate Research Program — May 2014 – Present
Applied Research Lab (ARL) - Metals and Ceramics Dept. — State College, PA

- Conducted proprietary materials research for the US Navy and outside contractors
- Performed experimental testing, including tribology, hardness, high-pressure, and tensile testing
- Assisted in development of a proprietary subroutine for modelling particle-impact dynamics
- Conducted material characterization, including SEM, EDS, and Corrosion Testing
- Researched innovative material consolidation techniques, including Cold Spray and Metal AM
- Contracted to conduct failure analysis studies and present final results verbally and through writing
- Designed and wrote algorithm, code, and user interface for software distributed to customers
- Wrote and presented company research posters and technical talks at conferences and symposiums

LEADERSHIP EXPERIENCE

Engineers Without Borders – Penn State Student Chapter
Head of Programs — May 2016 – Present

- Responsible for leading all EWB-PSU domestic and international projects. Responsibilities include leading meetings, overseeing task groups, adopting new projects, submitting grant applications, and communicating with EWB-USA HW and any partnering communities

Honduras Project Lead — May 2015 – May 2016

- Oversaw a project to implement a solar PV system to power a potable water well for the community of West End, Honduras

Presentations

- "Implementation of the Preston-Tonks-Wallace Plasticity Model for the Cold Spray Process."
  Oral presentation. Presented at the 2017 PSU ESM Today Graduate Research Symposium.
  - Awarded the First Place Oral Presentation
- "Use of Cold Spray Porous Coatings for Emergency Cooling of Reactor Vessels."
  Poster presentation. Presented at the 2017 PSU ESM Today Graduate Research Symposium
- "Production of Sintered Reaction Bonded Silicon Nitride."
  Poster presentation. Presented at the 2015 PSU Materials Day

Additional Skills

- Certified user of Penn State - Material Research Institute (MRI) facilities
- Professional experience in CAD design and FEA, including Catia V5, SolidWorks, and Abaqus
- Professional experience in: MatLab, LabView, and Microsoft Visual Studio
- Fluency creating professional documents with multi-media software (Photoshop, Premiere Pro, etc.)

Additional Accomplishments

- Student mentor for PSU's "Undergraduate Research Introduction to Science and Engineering" (U-RISE) program
- "Best Design Communication" award at the PSU Eng. Design Showcase
- "Boeing Outstanding Junior in Mechanical Engineering" Award
- "Best in Class" design for an Additive Manufacturing Eng. Design competition
- Member of ASME, AIAA, and Engineers Without Borders – USA
- Received over 20 Scholarships and Awards, including:
  - PSU Lashley Schp. in Engineering
  - PSU Anderson Schp. in Engineering
  - LGS Innovations Schp.
  - Evan Pugh Scholar Award
  - Gabron Schp. In Eng.
  - Pentz Mem Academic Excel Schp.
  - Edward Frymoyer Honors Schp.
  - Wharton Memorial Schp.